Article

SOURCE DATA | TRANSPARENT PROCESS | OPEN ACCESS

THE EMBO JOURNAL

Phosphorylation of phase-separated p62 bodies by ULK1 activates a redox-independent stress response

Ryo Ikeda[1,2], Daisuke Noshiro[3], Hideaki Morishita[1], Shuhei Takada[1], Shun Kageyama[1], Yuko Fujioka[3], Tomoko Funakoshi[1], Satoko Komatsu-Hirota[1], Ritsuko Arai[4], Elena Ryzhii[4], Manabu Abe[5], Tomoaki Koga[6], Hozumi Motohashi[7], Mitsuyoshi Nakao[6], Kenji Sakimura[5], Arata Horii[2], Satoshi Waguri[4], Yoshinobu Ichimura[1,*], Nobuo N Noda[3,**] & Masaaki Komatsu[1,***]

Abstract

NRF2 is a transcription factor responsible for antioxidant stress responses that is usually regulated in a redox-dependent manner. p62 bodies formed by liquid–liquid phase separation contain Ser349-phosphorylated p62, which participates in the redox-independent activation of NRF2. However, the regulatory mechanism and physiological significance of p62 phosphorylation remain unclear. Here, we identify ULK1 as a kinase responsible for the phosphorylation of p62. ULK1 colocalizes with p62 bodies, directly interacting with p62. ULK1-dependent phosphorylation of p62 allows KEAP1 to be retained within p62 bodies, thus activating NRF2. *p62*$^{S351E/+}$ mice are phosphomimetic knock-in mice in which Ser351, corresponding to human Ser349, is replaced by Glu. These mice, but not their phosphodefective *p62*$^{S351A/S351A}$ counterparts, exhibit NRF2 hyperactivation and growth retardation. This retardation is caused by malnutrition and dehydration due to obstruction of the esophagus and forestomach secondary to hyperkeratosis, a phenotype also observed in systemic *Keap1*-knockout mice. Our results expand our understanding of the physiological importance of the redox-independent NRF2 activation pathway and provide new insights into the role of phase separation in this process.

Keywords KEAP1; liquid–liquid phase separation; NRF2/NFE2L2; p62/SQSTM1; ULK1

Subject Category Autophagy & Cell Death

DOI 10.15252/embj.2022113349 | Received 20 December 2022 | Revised 2 May 2023 | Accepted 10 May 2023 | Published online 12 June 2023

The EMBO Journal (2023) 42: e113349

Introduction

Liquid–liquid phase-separated biomolecular condensates, liquid droplets play an important role in many biological processes, such as gene expression, protein translation, stress response, and protein degradation, by incorporating a variety of RNA and client proteins into their interior depending on the intracellular context (Alberti & Hyman, 2021). Autophagy is involved in the degradation of several cytoplasmic liquid droplets, including stress granules and P bodies, and defects in this process are thought to cause transition of these droplets to the solid phase, resulting in the development of intractable diseases such as neurodegenerative disorders and cancer (Woodruff *et al*, 2018; Noda *et al*, 2020). Of the droplets that have a unique biological function and are degraded by autophagy, p62 bodies (also called p62 droplets) are liquid droplets formed by liquid–liquid phase separation (LLPS) of p62 and its binding partners, ubiquitinated proteins (Sun *et al*, 2018; Zaffagnini *et al*, 2018). p62 bodies are involved in the regulation of intracellular proteostasis through their own autophagic degradation, and also contribute to the regulation of the major stress-response mechanism by sequestration of a client protein, kelch-like ECH-associated protein 1 (KEAP1) (Kirkin & Rogov, 2019; Faruk *et al*, 2021b).

Unc-51-like kinase 1 (ULK1) phosphorylates p62 at Ser407, inhibiting dimer formation of the ubiquitin-associated (UBA) domain of p62 (Isogai *et al*, 2011; Lim *et al*, 2015), and subsequent

1 Department of Physiology, Juntendo University Graduate School of Medicine, Tokyo, Japan
2 Department of Otolaryngology Head and Neck Surgery, Niigata University Graduate School of Medical and Dental Sciences, Niigata, Japan
3 Institute for Genetic Medicine, Hokkaido University, Sapporo, Japan
4 Department of Anatomy and Histology, Fukushima Medical University School of Medicine, Fukushima, Japan
5 Department of Animal Model Development, Brain Research Institute, Niigata University, Niigata, Japan
6 Department of Medical Cell Biology, Institute of Molecular Embryology and Genetics, Kumamoto University, Kumamoto, Japan
7 Department of Gene Expression Regulation, Institute of Development, Aging and Cancer, Tohoku University, Sendai, Japan
*Corresponding author. Tel: +81 3 5802 1028; E-mail: yichimu@juntendo.ac.jp
**Corresponding author. Tel: +81 11 706 7826; E-mail: nn@igm.hokudai.ac.jp
***Corresponding author. Tel: +81 3 5802 1029; E-mail: mkomatsu@juntendo.ac.jp

© 2023 The Authors. Published under the terms of the CC BY 4.0 license

phosphorylation of Ser403 by TBK1, CK2, TAK1, and ULK1 allows binding of ubiquitinated proteins (Matsumoto *et al*, 2011; Pilli *et al*, 2012; Lim *et al*, 2015; Kehl *et al*, 2019). These phosphorylation events are thought to promote LLPS (Sun *et al*, 2018; Zaffagnini *et al*, 2018). In the degradation of p62 bodies, the ULK1 protein kinase complex consisting of FIP200/RB1-inducible coiled-coil protein 1 (hereafter FIP200), ULK1, ATG13, and ATG101 is translocated onto the bodies by binding of the FIP200 Claw domain to p62 (Turco *et al*, 2019). Alternatively, the ULK1 protein kinase complex is recruited to p62 bodies through the interaction of FIP200 with TAX1BP1, which localizes at p62 bodies through the interaction with the p62 binding partner NBR1 (Turco *et al*, 2021). Subsequently, ATG proteins assemble around the bodies (Kageyama *et al*, 2021). In the end, the p62 bodies are surrounded by autophagosomes due to the wetting effect (Agudo-Canalejo *et al*, 2021) and the binding of LC3 or GABARAP to p62 on the isolation membrane (Kageyama *et al*, 2021), followed by lysosomal degradation.

KEAP1 is an adaptor protein of cullin 3 ubiquitin ligase for nuclear factor (erythroid-derived 2)-like 2 (NRF2), which is a key transcription factor for a series of genes encoding anti-oxidative proteins and enzymes (Yamamoto *et al*, 2018). In the canonical pathway, KEAP1 is inactivated by the modification of oxidants, and NRF2 is then activated via redox-dependent regulation (Yamamoto *et al*, 2018). This redox-dependent pathway has been shown to be important in redox, metabolism, and protein homeostasis, as well as in the regulation of inflammation and cellular protection against many pathological conditions (Yamamoto *et al*, 2018; Cuadrado *et al*, 2019). In addition to this canonical pathway, a specific region of p62 directly interacts with KEAP1, competitively preventing the interaction between KEAP1 and NRF2 (Komatsu *et al*, 2010). The phosphorylation of Ser349 located in the KEAP1-interacting region of p62 enhances the interaction of p62 with KEAP1, resulting in full activation of NRF2 independently of redox conditions (Ichimura *et al*, 2013). However, the kinase(s) and regulatory mechanism underlying the redox-independent pathway, as well as its physiological significance, remain unclear.

Herein, we show for the first time that ULK1 is a major kinase for Ser349 of p62, both *in vitro* and *in vivo*. ULK1 directly interacts with p62 and phosphorylates Ser349 of p62. ULK1 localizes in p62 bodies *in vitro* and *in vivo* in a FIP200-independent fashion. While this phosphorylation does not affect the influx of KEAP1 into p62 bodies, it inhibits KEAP1 outflow, keeping KEAP1 in the p62 bodies and activating NRF2. Knock-in mice with a phosphomimetic mutation, but not those with a phosphodefective mutation, exhibit persistent activation of NRF2, which causes hyperkeratosis and consequently obstruction of the esophagus and forestomach, and eventually severe growth retardation due to malnutrition. Taken together, these results indicate the physiological importance of the p62 body- and ULK1-dependent and redox-independent stress response.

Results

ULK1 directly interacts with and phosphorylates p62

To clarify whether the ULK1 kinase itself has an effect on the physical properties and physiological role of p62 bodies, we first studied the physical interaction of p62 with ULK1 or its yeast homolog Atg1 using high-speed atomic force microscopy (HS-AFM) (Fig 1). ULK1 has a serine–threonine kinase domain (KD) at the N-terminus and two microtubule interaction and transport (MIT1 and 2) domains at the C-terminus, all of which are conserved between yeast and mammals (Fig 1A). The KD and MIT1/2 domains are linked by an intrinsically disordered region (IDR) (Fig 1B). p62 contains an N-terminal Phox1 and Bem1p (PB1) domain and a C-terminal UBA domain, as well as several interacting regions such as the LC3-interacting region (LIR) and KEAP1-interacting region (KIR), located in an IDR between the PB1 and UBA domains (Fig 1A and B). We purified recombinant p62 (268–440 aa and 320–440 aa) and SNAP-tagged ULK1 and Atg1 (Fig 1C). HS-AFM of SNAP-ULK1 revealed that like Atg1, it contains two globular domains consisting of a KD and two tandem MIT domains, linked to each other with an IDR, (Kodera *et al*, 2021) (Fig EV1A, Movie EV1). Meanwhile, HS-AFM of p62 (268–440 aa) visualized a homodimeric structure, mediated by the dimerization of the UBA domain, that formed a hammer-shaped structure with IDRs wrapped around each other (Fig EV1B, Movie EV2). When each SNAP-ULK1 and SNAP-Atg1 was mixed with p62 (268–440 aa), the p62 homodimer directly bound to SNAP-ULK1 and SNAP-Atg1 via dynamic IDR-IDR and IDR-globular domain interactions (Figs 1D and E, and EV1C and D, Movies EV3 and EV4). Consistent with this, ULK1 and Atg1 directly phosphorylated recombinant p62 (268–440 aa and 320–440 aa) at Ser349 (Fig 1F). Although Ser403 was hardly phosphorylated (Fig 1F), it was also phosphorylated when mCherry-tagged full-length p62 was used (Fig 1F), indicating that the N-terminal PB1 domain of p62 is required for efficient Ser403 phosphorylation by ULK1 and Atg1. These data suggest that ULK1 directly interacts with and phosphorylates p62.

Figure 1. Molecular dynamics of ULK1 and p62.

A Domain structures of ULK1, Atg1, and p62. KD, kinase domain; MIT, microtubule interaction and transport domain; PB1, Phox1 and Bem1p domain; LIR, LC3-interacting region; KIR, KEAP1-interacting region; UBA, ubiquitin-associated.

B Three-dimensional structures of ULK1, Atg1, and p62 as predicted by Alphafold 2.

C CBB staining of purified p62 (268–440 aa), p62 (320–440 aa), SNAP-Atg1, and SNAP-ULK1.

D Successive HS-AFM images of p62_268–440 with SNAP-ULK1. Height scale: 0–3.5 nm; scale bar: 20 nm.

E Schematics showing the molecular characteristics observed by HS-AFM. Gray spheres, globular domains consisting of N-terminal KD and C-terminal MIT domain of ULK1; pink spheres, globular domains consisting of C-terminal UBA domain of p62; blue thick solid lines, IDRs.

F *In vitro* kinase assay. Purified recombinant p62 (268–440 aa), p62 (320–440 aa), or mCherry-p62 was incubated for 20 min at 30°C with purified SNAP-Atg1 or SNAP-ULK1 in the presence or absence of ATP. Reactions were then terminated by adding LDS sample buffer containing reducing agent, followed by immunoblot analysis with the indicated antibodies. As positive and negative controls, Huh-1 cell lysates treated with or without lambda protein phosphatase (λPP) were used. Data were obtained from three independent experiments. Asterisks show possible dimeric structures of p62 (268–440 aa), p62 (320–440 aa) and mCherry-p62.

Source data are available online for this figure.

 © 2023 The Authors

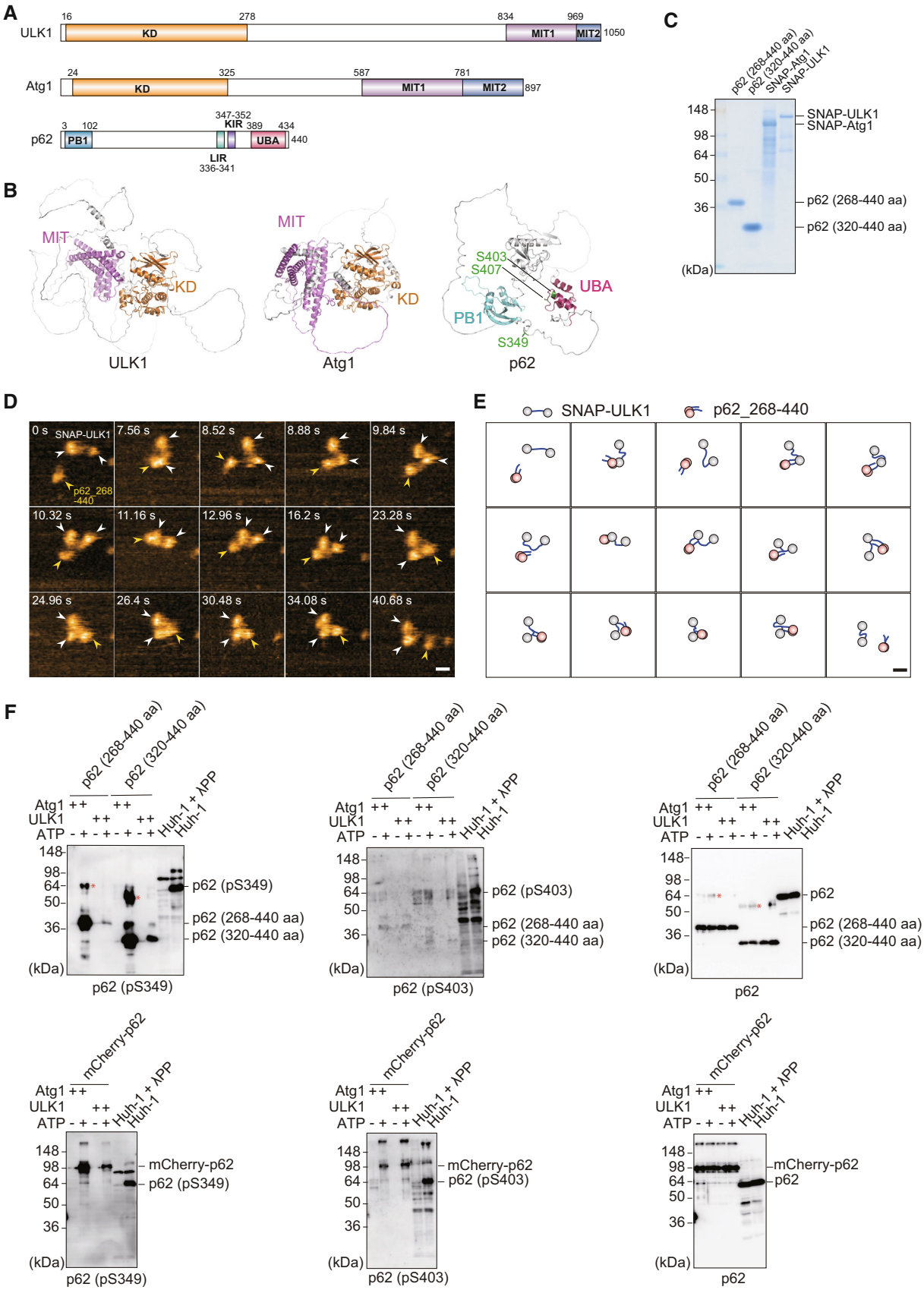
A
ULK1
16
278
834
969
1050
KD
MIT1
MIT2
Atg1
24
325
587
781
897
p62
3
102
347-352
KIR
389
434
440
PB1
UBA
LIR
336-341
B
MIT
KD
ULK1
Atg1
S403
S407
UBA
PB1
S349
p62
C
p62 (268-440 aa)
p62 (320-440 aa)
SNAP-Atg1
SNAP-ULK1
148
98
64
50
36
(kDa)
SNAP-ULK1
SNAP-Atg1
p62 (268-440 aa)
p62 (320-440 aa)
D
0 s
SNAP-ULK1
p62_268-440
7.56 s
8.52 s
8.88 s
9.84 s
10.32 s
11.16 s
12.96 s
16.2 s
23.28 s
24.96 s
26.4 s
30.48 s
34.08 s
40.68 s
E
SNAP-ULK1
p62_268-440
F
p62 (268-440 aa)
p62 (320-440 aa)
Atg1
ULK1
ATP
Huh-1 + λPP
Huh-1
p62 (pS349)
p62 (pS403)
p62
mCherry-p62

Figure 1.

Localization of ULK1 in p62 bodies

p62 undergoes LLPS upon interaction with ubiquitinated proteins *in vitro*, forming p62 condensates (Sun *et al*, 2018). We examined whether SNAP-Atg1 and SNAP-ULK1 associate with p62 condensates *in vitro*. Consistent with previous reports (Sun *et al*, 2018; Zaffagnini *et al*, 2018; Kageyama *et al*, 2021), mixing mCherry-p62 with linear octa-ubiquitin (8xUb) resulted in the formation of condensates (Fig 2A). Their size was markedly increased by phosphomimetic p62 mutations (S403E and S407E) that are known to increase the binding affinity of p62 to ubiquitin (Matsumoto *et al*, 2011; Pilli *et al*, 2012; Lim *et al*, 2015), compared with a slight increase in the S349E phosphomimetic mutation (Fig 2A). SNAP-Atg1 and SNAP-ULK1 were recruited to both wild-type and phosphomimetic p62 condensates when all were incubated together (Figs 2B and EV2A), but not when SNAP-tag or protein kinase A (PKA) instead of SNAP-ULK1 was used (Fig EV2B). These results imply that both Atg1 and ULK1 specifically associate with p62 even in the droplet form.

We next studied the localization of ULK1 in Huh-1 cells. Immunofluorescence analysis with an anti-ULK1 antibody showed a significant signal of ULK1 in p62 bodies, which was diminished by ULK1 depletion (Fig 2C, Appendix Fig S1). Together with FIP200, ATG13, and ATG101, ULK1 forms an initiation kinase complex for autophagosome formation (Lin & Hurley, 2016), and p62 interacts with FIP200 through the Claw domain (Turco *et al*, 2019), raising the possibility that the localization of ULK1 to p62 bodies is indirect and depends on the interaction of p62 with FIP200. To test this hypothesis, we developed *FIP200*-deficient Huh-1 cells (Appendix Fig S1). Remarkably, we observed ULK1 localization to p62 bodies even in these cells, and ULK1 signal intensity was significantly higher than in wild-type Huh-1 cells (Fig 2C), probably due to increased ULK1 protein in the *FIP200*-knockout cells. Exogenously expressed green fluorescent protein (GFP)-tagged ULK1 and ULK2 also localized on p62 bodies regardless of the presence of FIP200, but not in the case of GFP-LATS1, an irrelevant serine–threonine-protein kinase (Figs 2D and EV3A). An *in vitro* binding assay using purified p62, ULK1, and FIP200 Claw showed that ULK1 alone bound to p62 and that FIP200 did not interfere with ULK1 for p62-binding (Fig EV3B and C). Correlative light and electron microscopy with Huh-1 cells harboring GFP-ULK1 revealed that GFP-ULK1 localizes on round structures composed of filamentous assemblies; these structures were previously identified as p62 bodies (Jakobi *et al*, 2020; Kageyama *et al*, 2021) (Fig 2E). Taken together, these data suggest that ULK1 localizes in p62 bodies through a direct ULK1-p62 interaction.

Significance of ULK1 within p62 bodies

In addition to Ser349 in KIR of p62, ULK1 phosphorylates Ser403 and Ser407 within the UBA domain of p62 (Ro *et al*, 2014; Lim *et al*, 2015). It is unclear whether the phosphorylation of the UBA domain affects Ser349 and *vice versa*. To address this issue, we expressed the wild-type p62, $p62^{S349E}$ (S349-phosphomimetic) (Ichimura *et al*, 2013), $p62^{S349A}$ (S349-phosphodefective) (Ichimura *et al*, 2013), $p62^{S403E\ S407E}$ (S403E and S407E-phosphomimetic), or $p62^{S403A\ S407A}$ (S403A and S407A-phosphodefective) mutant in *p62*-deficient Huh-1 cells and investigated the phosphorylation states of Ser349, Ser403, and Ser407. As shown in Appendix Fig S2, while the $p62^{S349E}$ mutant had no effect on the phosphorylation of the UBA domain, the $p62^{S403E\ S407E}$ mutant enhanced the phosphorylation of Ser349. Considering that the phosphorylation of S403 and S407 is thought to promote the LLPS of p62, it is plausible that Ser349 phosphorylation of p62 occurs within p62 bodies.

Next, to investigate the significance of ULK1 and ULK2 within p62 bodies, we utilized MRT68921, which is the most potent inhibitor of ULK1 and ULK2, with IC_{50} values of 2.9 and 1.1 nM, respectively (Petherick *et al*, 2015). As predicted, the treatment of Huh-1 cells with 2.5 μM MRT68921 decreased not only the level of phosphorylated ATG13, but also those of the Ser349- and Ser403-phosphorylated p62 forms (Fig 3A). Even when we used a lower concentration of MRT68291 (1 μM), the levels of the Ser349- and Ser403-phosphorylated p62 forms decreased to the same degree (Fig EV4A). Similar results were obtained with ULK-101, another inhibitor of ULK1 and ULK2 (Martin *et al*, 2018) (Fig EV4A).

We observed extensive colocalization of the Ser403-phosphorylated form in p62 bodies (Fig 3B). The signal intensity of Ser403-phosphorylated p62 in p62 bodies became weaker when

Figure 2. Localization of ULK1 on p62 bodies.

A *In vitro* formation of p62-8xUb condensates. 10 μM SNAP-8xUb labeled with Alexa Fluor 649 was mixed with 10 μM mCherry-p62 wild-type, mCherry-$p62^{S403E\ S407E}$, or mCherry-$p62^{S349E}$ and observed by fluorescence microscopy. Scale bars: 20 μm. The graph indicates the quantified area of p62 condensates formed by wild-type or mutant p62. Data are means ± s.d. of wild-type p62, $p62^{S403E,\ S407E}$ and $p62^{S349E}$ condensates (n = 4). Statistical analysis was performed by Šidák's test after one-way ANOVA.

B *In vitro* formation of p62-8xUb-Atg1 or ULK1 condensates. 10 μM mCherry-p62 wild-type, or mCherry-$p62^{S403E\ S407E}$ and 10 μM 8xUb labeled with Alexa Fluor 649 were mixed with 0.2 μM SNAP-Atg1, or SNAP-ULK1 labeled with Alexa Fluor 488 and observed by fluorescence microscopy. Scale bars: 10 μm.

C Immunofluorescence microscopy. Wild-type, *FIP200*- or *ULK1*-knockout Huh-1 cells were immunostained with indicated antibodies. The mean fluorescence intensities of ULK1 on p62 bodies per cell were quantified in each genotype (n = 249 cells). Horizontal bars indicate medians, boxes the interquartile range (25th–75th percentiles) and whiskers 1.5× the interquartile range; outliers are plotted individually. Statistical analysis was performed by Šidák's test after one-way ANOVA. Scale bars, 10 μm (main panels), 1 μm (inset panels).

D Immunofluorescence microscopy. Wild-type and *FIP200*-knockout Huh-1 cells were transfected with GFP-ULK1 or GFP-ULK2 and immunostained with anti-p62 antibody. The mean fluorescence intensities of ULK1 on p62 bodies in each cell were quantified for each genotype (n = 79 cells). Horizontal bars indicate medians, boxes indicate interquartile range (25th–75th percentiles), and whiskers indicate 1.5× interquartile range; outliers are plotted individually. Statistical analysis was performed by Welch's t-test. Scale bars, 10 μm (main panels), 1 μm (inset panels).

E Correlative light and electron microscopy (CLEM) of Huh-1 cells expressing GFP-ULK1. Images of GFP-ULK1, corresponding electron micrograph (EM) images, and the merging of both (CLEM) are shown. Areas 1 and 2 are magnified in the bottom. Arrowheads indicate GFP-ULK1-positive p62 bodies. Scale bars, 5 μm (upper panel), 1 μm (lower panels), and 100 nm (insets of lower panels).

Source data are available online for this figure.

 © 2023 The Authors

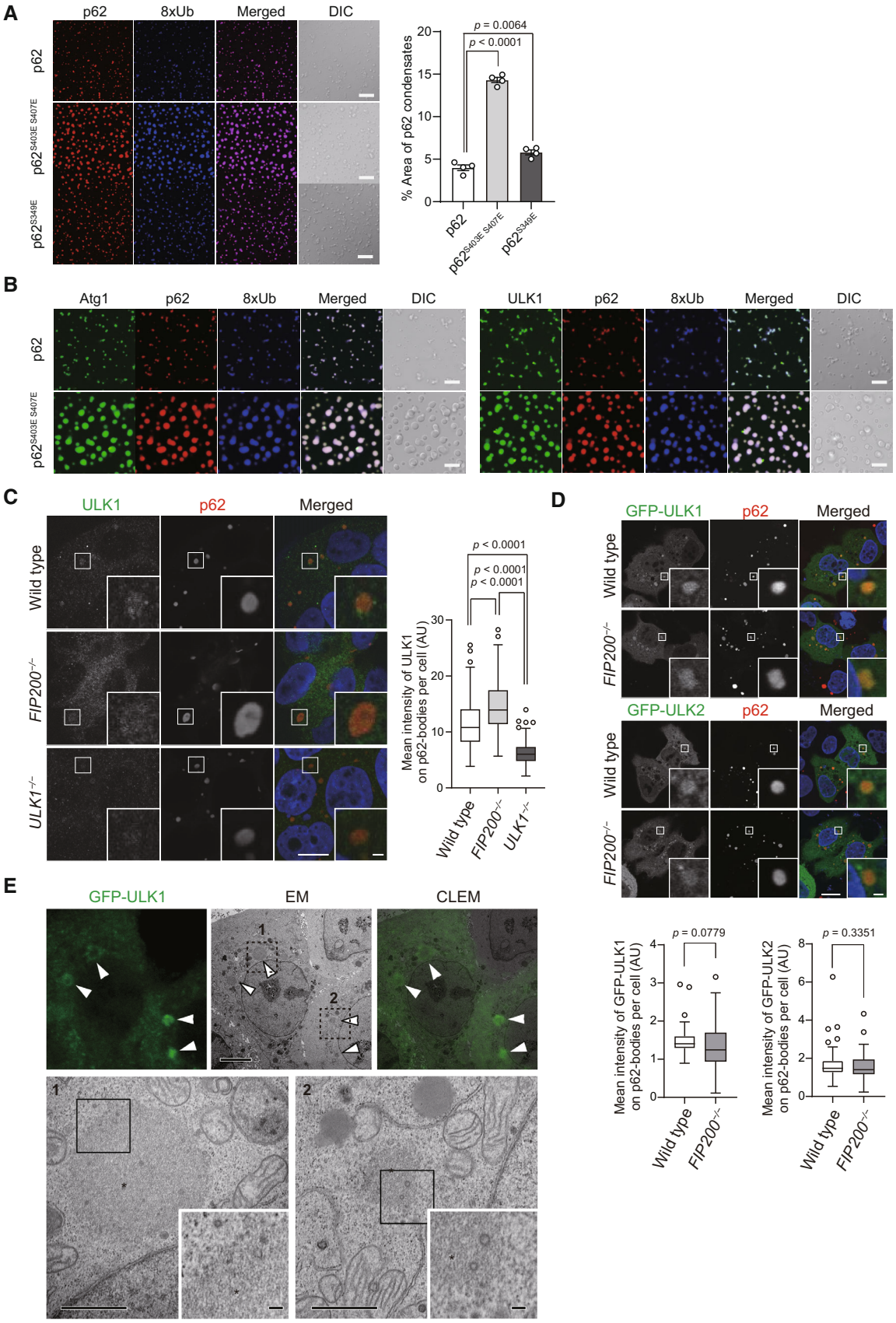
A
p62
8xUb
Merged
DIC
p62
p62S403E S407E
p62S349E
% Area of p62 condensates
p = 0.0064
p < 0.0001
B
Atg1
p62
8xUb
Merged
DIC
ULK1
C
ULK1
Wild type
FIP200−/−
ULK1−/−
Mean intensity of ULK1 on p62-bodies per cell (AU)
p < 0.0001
D
GFP-ULK1
GFP-ULK2
Mean intensity of GFP-ULK1 on p62-bodies per cell (AU)
Mean intensity of GFP-ULK2 on p62-bodies per cell (AU)
p = 0.0779
p = 0.3351
E
GFP-ULK1
EM
CLEM

Figure 2.

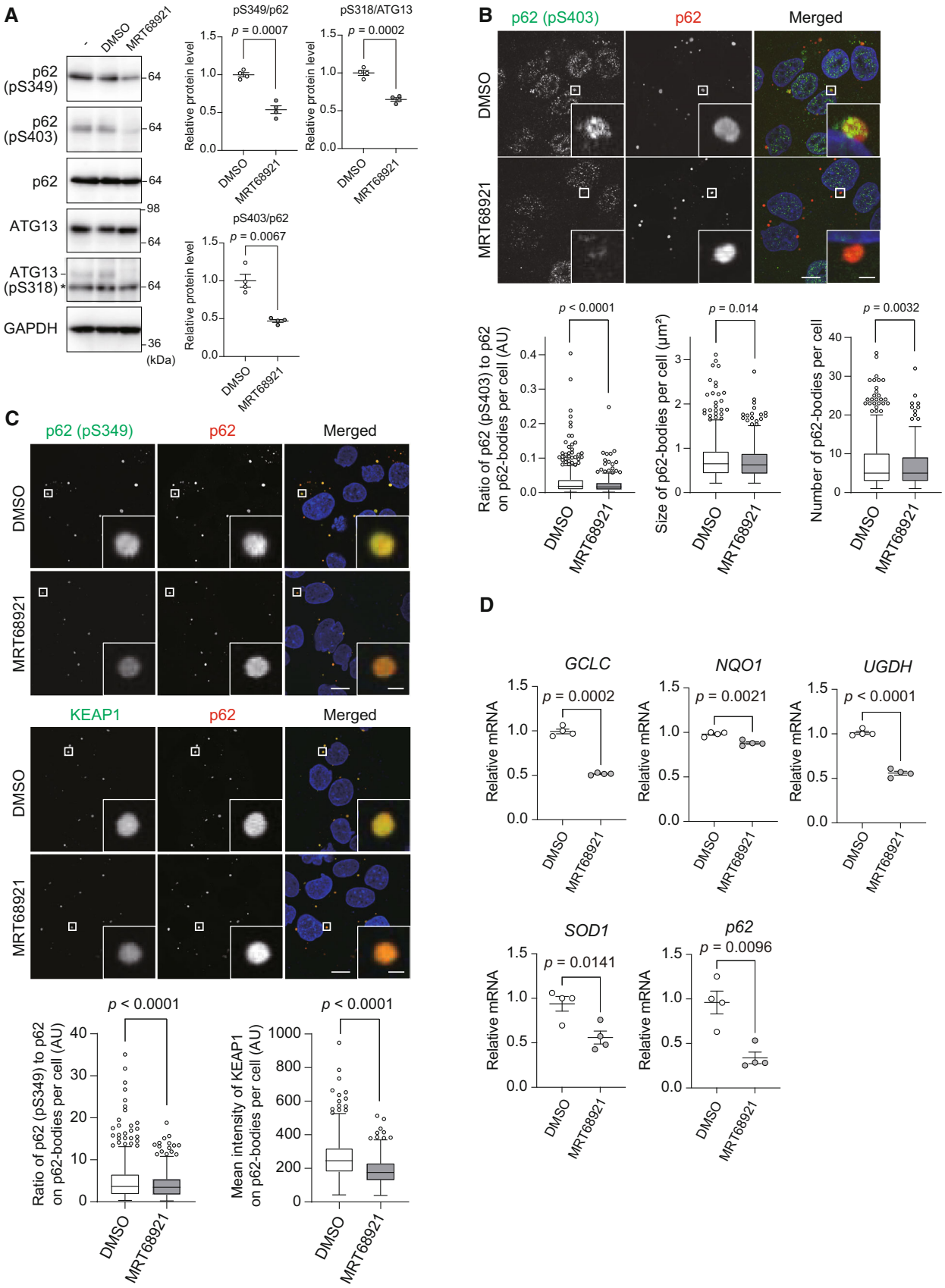

Figure 3.

© 2023 The Authors

Figure 3. Significance of p62 phosphorylation by ULK1 and ULK2.

A Immunoblot analysis. Huh-1 cells were treated with or without 2.5 μM MRT68921 for 6 h, and the cell lysates were subjected to immunoblot analysis with indicated antibodies. The asterisk indicates non-specific bands. Data shown are representative of three separate experiments. Bar graphs show the results of quantitative densitometric analysis of Ser349- or Ser403-phosphorylated p62 forms relative to total p62 (n = 3), and of Ser318-phosphorylated ATG13 relative to total ATG13 (n = 3). Data are means ± s.e. Statistical analysis was performed by Welch's t-test.

B Immunofluorescence microscopy. Huh-1 cells were treated with or without 2.5 μM MRT68921 for 6 h and immunostained with the indicated antibodies. The ratio of p62 (p-S403) to p62 on p62 bodies and the size and number of p62 bodies in each cell were quantified (n = 500 cells). Horizontal bars indicate medians, boxes indicate interquartile range (25th–75th percentiles), and whiskers indicate 1.5× interquartile range; outliers are plotted individually. Statistical analysis was performed by Welch's t-test. Scale bars, 10 μm (main panels), 1 μm (inset panels).

C Immunofluorescence microscopy. Huh-1 cells were treated with or without 2.5 μM MRT68921 for 6 h and immunostained with the indicated antibodies. The ratio of p62 (p-S349) to p62 and the signal intensity of KEAP1 on p62 bodies in each cell were quantified (n = 500 cells). Horizontal bars indicate medians, boxes indicate interquartile range (25th–75th percentiles), and whiskers indicate 1.5× interquartile range; outliers are plotted individually. Statistical analysis was performed by Welch's t-test. Scale bars, 10 μm (main panels), 1 μm (inset panels).

D Gene expression of NRF2 targets. Total RNAs were prepared from Huh-1 cells treated with or without 2.5 μM MRT68921 for 6 h. Values were normalized against the amount of mRNA in non-treated Huh-1 cells. qRT-PCR analyses were performed as technical replicates on each biological sample. Data are means ± s.e. Statistical analysis was performed by two-sided Welch's t-test.

Source data are available online for this figure.

Huh-1 cells were treated with MRT68921 (Fig 3B). MRT68921 treatment slightly but significantly decreased both the size and number of p62 bodies (Fig 3B). These results suggest that while ULK1 and ULK2 contribute to the LLPS of p62 through the phosphorylation of Ser403 of p62, the dephosphorylation of Ser403 within p62 bodies hardly has an effect on already formed p62 bodies.

Next, we tested whether inhibition of ULK1 and ULK2 affected KEAP1-localization within p62 bodies. Huh-1 cells were cultured in the presence or absence of MRT68921 and immunostained with anti-p62 and anti-Ser349-phosphorylated p62-specific antibodies. The p62 bodies in Huh-1 cells contained the Ser349-phosphorylated form (Fig 3C). Upon exposure to MRT68921, the signal intensities of phosphorylated p62 on p62 bodies markedly decreased (Fig 3C). Double immunofluorescence analysis with anti-p62 and anti-KEAP1 antibodies showed extensive localization of KEAP1 in the p62 bodies (Fig 3C). The signal intensity of KEAP1 in the bodies was significantly attenuated by treatment with MRT68921 (Fig 3C), suggesting release of KEAP1 from the bodies to the cytoplasm and subsequent NRF2 inactivation. Indeed, the gene expression of NRF2 targets such as glutamate-cysteine ligase catalytic subunit (*GCLC*), NAD(P)H quinone dehydrogenase 1 (*NQO1*), UDP-glucose 6-dehydrogenase (*UGDH*), superoxide dismutase 1 (*SOD1*), and *p62* itself was decreased by MRT68921 or ULK-101 treatment (Figs 3D and EV4B). These data suggest that ULK1 and ULK2 in p62 bodies contribute to the activation of NRF2 by phosphorylating p62 at Ser349 and promoting sequestration of KEAP1 within p62 bodies.

Dynamics of KEAP1 in S349-phosphorylated p62 bodies

In the next series of experiments, we sought to determine whether Ser349 phosphorylation of p62 affects KEAP1 dynamics in p62 bodies. To do this, we generated *p62 KEAP1* double-knockout Huh-1 cells (Appendix Fig S1) and expressed GFP-tagged wild-type p62, phosphomimetic $p62^{S349E}$ (Ichimura *et al*, 2013), phosphodefective $p62^{S349A}$ (Ichimura *et al*, 2013), or KEAP1 interaction-defective $p62^{T350A}$ (Komatsu *et al*, 2010) together with mCherry or mCherry-tagged KEAP1. The fluorescence analysis revealed that in the absence of mCherry-KEAP1, wild-type GFP-p62 and all GFP-p62 mutants formed round, liquid droplet-like structures (Fig 4A). When we coexpressed wild-type GFP-p62 or the mutants with mCherry-KEAP1 in the double knockout Huh-1 cells, mCherry-KEAP1 colocalized well with GFP-p62-positive structures except those composed of GFP-$p62^{T350A}$ (Fig 4A). We measured the circularity of each GFP-p62-positive structure composed of wild-type p62 or the mutants in the presence or absence of mCherry-KEAP1. Circularity values close to 1 were associated with liquid droplets, while lower values

Figure 4. Dynamics of KEAP1 in p62 bodies.

A Fluorescence microscopy. GFP-p62, GFP-$p62^{S349E}$, GFP-$p62^{S349A}$, or GFP-$p62^{T350A}$ were co-transfected with mCherry or mCherry-KEAP1 into Huh1 *p62 KEAP1* double-knockout cells. Twenty-four hours after transfection, the fluorescence images were observed.

B Circularity of p62 bodies. The circularity of p62 bodies in each cell was quantified (n = 150 cells). Horizontal bars indicate medians, boxes indicate interquartile range (25th–75th percentiles), and whiskers indicate 1.5× interquartile range; outliers are plotted individually. Statistical analysis was performed by two-sided Welch's t-test. Scale bar: 2 μm.

C The ratio of the mean signal intensity of mCherry-KEAP1 on p62 bodies to that of the cellular area in each type of Huh-1 *p62 KEAP1* double-knockout cell expressing mCherry-KEAP1 (n = 150 cells). Horizontal bars indicate medians, boxes indicate interquartile range (25th–75th percentiles), and whiskers indicate 1.5× interquartile range; outliers are plotted individually. Statistical analysis was performed by Šidák's test after one-way ANOVA.

D *In vitro* formation of p62-KEAP1-8xUb condensates. 5 μM SNAP-KEAP1 labeled with SNAP-Surface Alexa Fluor 488 was premixed with 10 μM mCherry-p62 wild-type, or mCherry-p62 mutants before mixing with 10 μM SNAP(649)-8xUb. Scale bars: 20 μm.

E FRAP analyses of mCherry-KEAP1 localized in p62 bodies comprised of GFP-$p62^{S349E}$ or GFP-$p62^{S349A}$. The half-time of recovery (*t50*) and mobile fraction (MF) of mCherry-KEAP1 was measured by FRAP of whole p62 bodies (n = 7). Data are means ± s.d. Statistical analysis was performed by two-sided Welch's t-test.

F FLIP analyses of mCherry-KEAP1 localized in p62 bodies comprised of GFP-$p62^{S349E}$ or GFP-$p62^{S349A}$. The fluorescence loss of mCherry-KEAP1 in GFP-p62 bodies (n = 14) was measured 30 min after photobleaching over a large area of cells.

G FRAP analyses of mCherry-KEAP1 localized in p62 bodies comprised of GFP-$p62^{S349E}$ or GFP-$p62^{S349A}$. *t50* and MF of mCherry-KEAP1 were measured by FRAP of the central portions of p62 bodies (n = 10). Data are means ± s.d. Statistical analysis was performed by two-sided Welch's t-test.

Source data are available online for this figure.

© 2023 The Authors

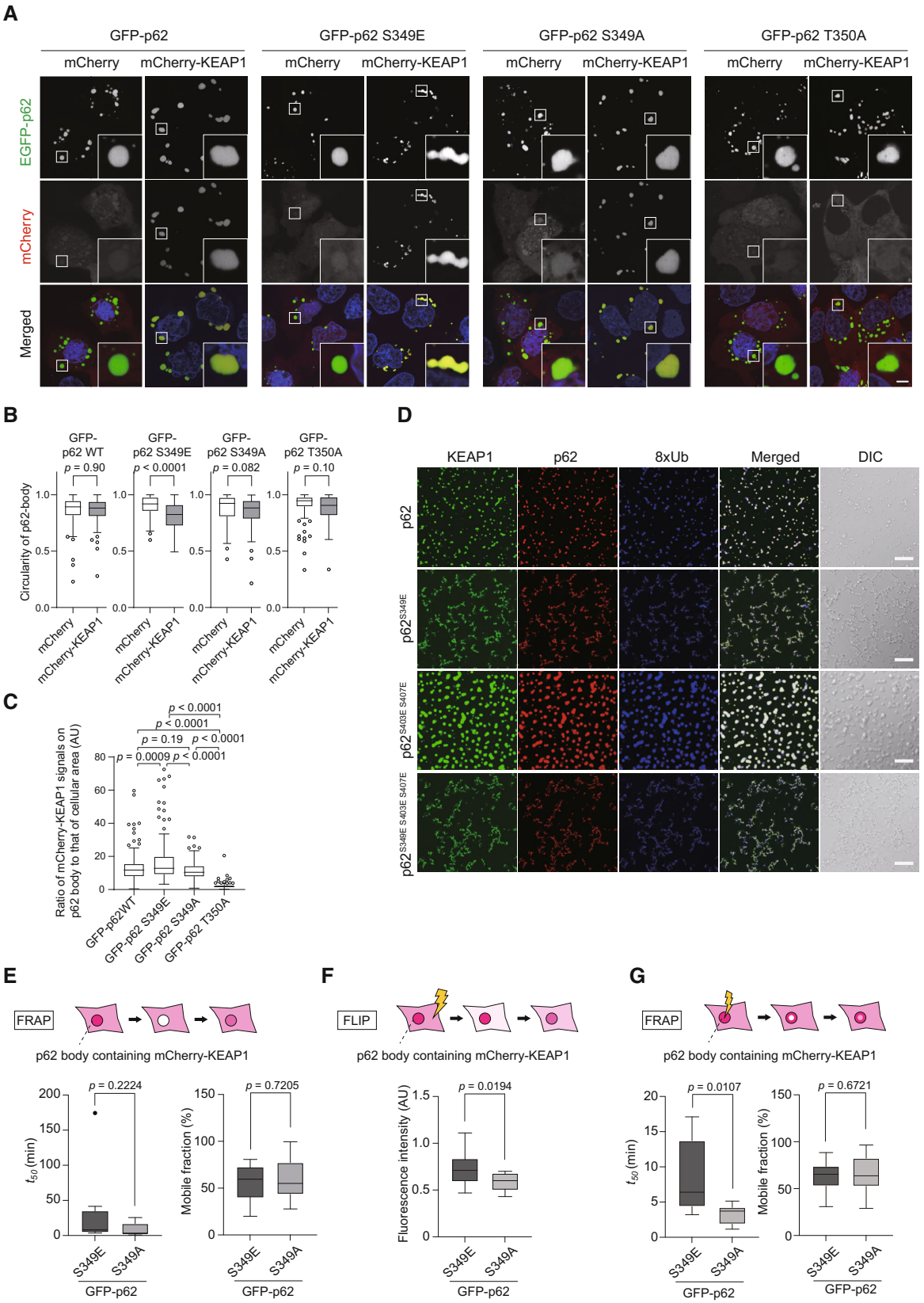

Figure 4.

© 2023 The Authors

correlated with gels or aggregates (Strom *et al*, 2017; Faruk *et al*, 2021a). In the absence of mCherry-KEAP1, all GFP-p62-positive structure values were close to 1 (Fig 4B), suggesting that they were liquid droplets. Remarkably, the circularity of GFP-p62^{S349E} bodies but not others was significantly decreased when these bodies colocalized with mCherry-KEAP1 (Fig 4B). We also measured the signal intensity of mCherry-KEAP1 on p62 bodies consisting of wild-type p62 or a series of different mutants and found that the intensity of mCherry-KEAP1 on p62^{S349E} bodies was higher than that on wild-type p62 and p62^{S349A} bodies (Fig 4C). Meanwhile, there was no significance difference in mCherry-KEAP1 intensity between wild-type p62 and p62^{S349A} bodies (Fig 4C). Furthermore, an *in vitro* LLPS assay revealed that introduction of the S349E mutation in p62 wild-type or p62$^{S403E\ S407E}$ resulted in the formation of amorphous aggregates rather than liquid droplets, but only in the presence of KEAP1 (Fig 4D, Appendix Fig S3). These data suggest that strong binding of KEAP1 to p62 as a result of the S349E mutation changes the biophysical properties of p62 bodies.

We hypothesized that once mCherry-KEAP1 was incorporated into S349-phosphorylated p62 bodies, KEAP1 efflux from the bodies would be significantly reduced due to the close interaction between the phosphorylated p62 and KEAP1. To prove this, we used fluorescence recovery after photobleaching (FRAP) and fluorescence loss in photobleaching (FLIP) (Ishikawa-Ankerhold *et al*, 2012) to evaluate KEAP1 influx and efflux into p62 bodies consisting of GFP-p62^{S349E} or p62^{S349A}. To measure the influx of mCherry-KEAP1 into GFP-p62 bodies, the whole fluorescence of mCherry-KEAP1 in GFP-p62^{S349E} or p62^{S349A} bodies was photobleached, and the fluorescence recovery was measured. It is common to characterize molecular dynamics in FRAP experiments by the half-time of recovery (*t50*) and the mobile fraction (Reits & Neefjes, 2001). Based on these parameters, the influx of mCherry-KEAP1 from the surrounding environment was comparable between p62^{S349E} and p62^{S349A} bodies (Fig 4E, Movies EV5 and EV6). Next, to examine the efflux of mCherry-KEAP1 from GFP-p62 bodies, we carried out FLIP analysis. When approximately 80% of the cellular region is photobleached, the fluorescent signal in the cytoplasm is transiently reduced, followed by a gradual recovery due to influx from the nonbleached region. If there is an outflow of mCherry-KEAP1 from p62 bodies, the fluorescence intensity of mCherry-KEAP1 within p62 bodies in the non-bleached area should decrease after photobleaching. While the signal intensity of mCherry-KEAP1 in p62^{S349A} bodies decreased to about 58.2 ± 0.05% of the baseline value at 30 min after photobleaching, it remained higher (72.0 ± 0.07%) in the case of p62^{S349E} bodies (Fig 4F, Movies EV7 and EV8). Finally, to investigate the inner fluidity of mCherry-KEAP1 in GFP-p62 bodies, we measured the fluorescence recovery of mCherry-KEAP1 after photobleaching of the central portion of GFP-p62 bodies. The *t50* of mCherry-KEAP1 in p62^{S349E} bodies was 8.51 ± 4.83 min, which was much slower than that seen with p62^{S349A} bodies (3.32 ± 1.23 min) (Fig 4G, Movies EV9 and EV10). Taken together, these results suggest that Ser349 phosphorylation of p62 results in the retention of KEAP1 in p62 bodies, and when this sequestration is prolonged, the inner fluidity of these bodies is decreased.

Physiological significance of Ser349 phosphorylation of p62 in mice

To clarify the physiological role of Ser349 phosphorylation of p62 *in vivo*, we generated knock-in mice that expressed p62 in which Ser351 (corresponding to human Ser349) was replaced by Glu (*p62*$^{S351E/+}$ mice) or Ala (*p62*$^{S351A/+}$ mice). Initially, we tried to use the CRISPR/Cas9 system to generate both knock-in mice, but could obtain only *p62*$^{S351A/+}$ mice. We therefore attempted to use prime editing, a recently developed system, to generate *p62*$^{S351E/+}$ mice using mouse embryonic stem cells (mES cells) (Anzalone *et al*, 2019). Even with this method, however, we were unable to obtain chimeric mice with high chimerism. We did succeed in generating a male chimeric mouse with low chimerism and germline transmission. *In vitro* fertilization using sperm from the chimeric mouse was performed to obtain a sufficient number of heterozygotes for the experiments. The resulting *p62*$^{S351E/+}$ mice showed severe growth retardation and mild hepatomegaly at P12 and P15 (Fig 5A–C), which is probably why knock-in mice could not be obtained by the above method. RNAseq analysis of wild-type and *p62*$^{S351E/+}$ mouse livers demonstrated increased gene expression of NRF2 targets (Fig 5D). Consistent with these results, real-time PCR analysis showed that the gene expression of NRF2 targets such as *glutathione S-transferase Mu 1* (*Gstm1*), *Nqo1*, *Ugdh*, and *p62* was much higher in the liver of *p62*$^{S351E/+}$ mice than in wild-type mice (Fig 5E). We also found that the levels of GSTM1, NQO1, and UGDH, and the nuclear level of NRF2, were markedly higher in

Figure 5. Physiological significance of p62 phosphorylation at S351 in mice.

A External appearance of *p62*$^{+/+}$ and *p62*$^{S351E/+}$ mice at postnatal days (P) 12 and 15.

B, C Body weight (g) (B) and liver weight (% of body weight) (C) of *p62*$^{+/+}$ (n = 4 at P12, n = 10 at P15) and *p62*$^{S351E/+}$ mice (n = 4). Data are means ± s.e. Statistical analysis was performed by Tukey's test after one-way ANOVA.

D RNA-seq analysis of livers of *p62*$^{+/+}$ and *p62*$^{S351E/+}$ mice at P19 (n = 3). Volcano plots of differentially expressed genes in *p62*$^{+/+}$ versus *p62*$^{S351E/+}$ mice (red points: FDR < 0.05 and log2FC > 1, blue points: FDR < 0.05 and log2FC < −1). Green points are the targets of transcription factor NRF2.

E Gene expression of NRF2 targets. Total RNAs were prepared from mouse livers of *p62*$^{+/+}$ (n = 10) and *p62*$^{S351E/+}$ (n = 4) mice at P15. Data are means ± s.e. Statistical analysis was performed by Welch's t-test.

F Immunoblot analysis of *p62*$^{+/+}$ (n = 7) and *p62*$^{S351E/+}$ (n = 3) mice at P19. Liver homogenates were subjected to immunoblot analysis with the indicated antibodies. Bar graphs show the results of quantitative densitometric analysis. Data are means ± s.e. Statistical analysis was performed by Welch's t-test. Note that both faster and slower migrating bands in the KEAP1 blot represent translational products from the *Keap1* gene.

G, H Hematoxylin and eosin (HE) staining (G) and immunohistochemical analysis of NQO1 (H) of livers from *p62*$^{+/+}$ and *p62*$^{S351E/+}$ mice at P19. Scale bars, 100 μm (low magnification panels), and 10 μm (high magnification panels).

I Serum levels of aspartate aminotransferase (AST), alanine aminotransferase (ALT), glucose, total cholesterol, blood urea nitrogen (BUN), and creatinine from *p62*$^{+/+}$ (n = 4 at P12, n = 10 at P15) and *p62*$^{S351E/+}$ (n = 4) mice at P12 and P15 were measured. IU/l, international units/liter. Data are means ± s.e. Statistical analysis was performed by Tukey's test after one-way ANOVA.

Source data are available online for this figure.

© 2023 The Authors

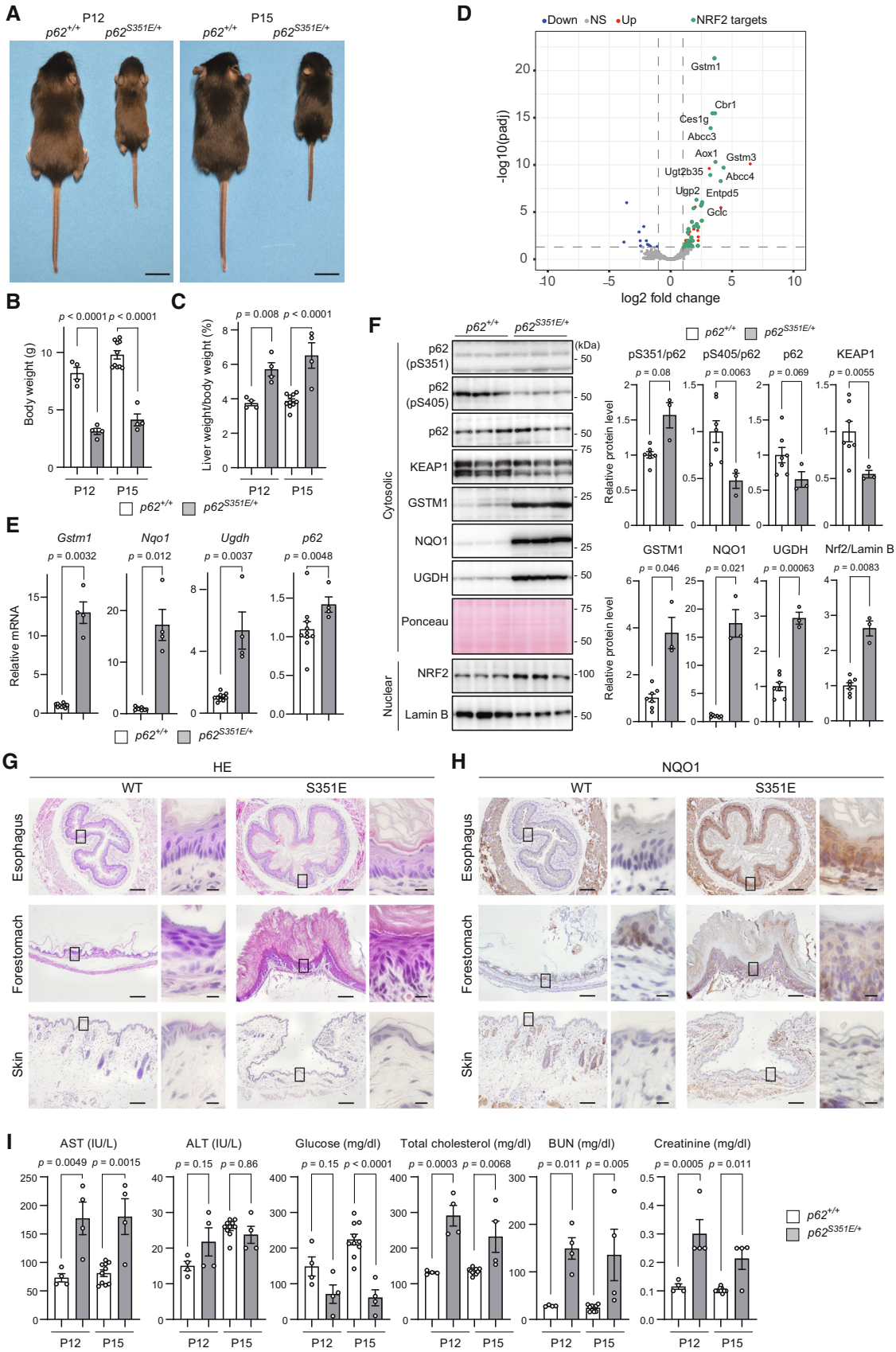

Figure 5.

© 2023 The Authors

p62$^{S351E/+}$ mice than in wild-type mice (Fig 5F). KEAP1 is incorporated into p62 bodies (Kageyama *et al*, 2021), and the complex of KEAP1 and p62 is degraded by autophagy (Taguchi *et al*, 2012). Therefore, the phosphorylation of p62 at Ser349, which increases the binding affinity to KEAP1, should promote the degradation of KEAP1. In fact, the level of KEAP1 was lower in *p62*$^{S351E/+}$ mice compared with that in wild-type mice (Fig 5F). These results indicate that the expression of *p62*^{S351E} at half the level of endogenous *p62* is sufficient for KEAP1 inactivation and subsequent NRF2 activation *in vivo*. Anatomical analysis revealed that the forestomach wall of *p62*$^{S351E/+}$ mice was obviously thickened compared with that of wild-type mice (Appendix Fig S4). Hematoxylin and eosin (HE) staining indicated that the esophagus and forestomach of *p62*$^{S351E/+}$ mice had a remarkably thicker stratum corneum than those of wild-type mice, but such differences were not observed in the skin (Fig 5G). In the forestomach, the epithelial layers below the stratum corneum were slightly thicker in *p62*$^{S351E/+}$ mice than in wild-type mice, but this was not evident in the esophagus. Immunohistochemistry (IHC) revealed that in the epithelia of the esophagus and forestomach, the intensity of NQO1 was higher in *p62*$^{S351E/+}$ mice than in wild-type mice (Fig 5H). The staining of the cell proliferation marker Ki-67 showed no significant difference between mutant and wild-type organs (data not shown). Serum data from *p62*$^{S351E/+}$ mice indicated a slightly but significantly elevated aspartate aminotransferase level, signs of malnutrition (low blood glucose and high cholesterol), and signs of dehydration (increased blood urea nitrogen and creatinine) (Fig 5I). These results strongly suggested that *p62*$^{S351E/+}$ mice are a phenocopy of *Keap1*-deficient mice (Wakabayashi *et al*, 2003) and that impaired nutritional intake due to hyperkeratosis in the esophagus and forestomach could be the primary cause of the severe phenotype of *p62*$^{S351E/+}$ mice. In striking contrast to these mice, *p62*$^{S351A/+}$ and *p62*$^{S351A/S351A}$ mice were fertile and showed no obvious growth retardation (Fig EV5A–C). Morphological and biochemical analyses indicated no differences in phenotypes (including NRF2 activation) between wild-type and *p62*$^{S351A/S351A}$ mice (Fig EV5D–G), implying that Ser351 phosphorylation of p62 is unnecessary for mouse development and survival. Taken together, these results indicate that Ser351 phosphorylation of p62 is physiologically important for the control of NRF2 activity *in vivo*, most likely by regulating the redox-independent KEAP1-NRF2 pathway.

Discussion

The ULK1 kinase complex functions as the most upstream factor in autophagosome formation (Noda & Fujioka, 2015; Lin & Hurley, 2016). In *Saccharomyces cerevisiae*, nutrient deprivation causes phosphatase-induced dephosphorylation of Atg13, which results in the formation of higher order structures of the Atg1 kinase complex (the ULK1 kinase complex in mammals) and subsequently the formation of a liquid-droplet, pre-autophagosomal structure (Yamamoto *et al*, 2016; Fujioka *et al*, 2020). Nutrient starvation activates the ULK1 kinase complex, which phosphorylates ATG proteins, including Beclin 1 (Russell *et al*, 2013), ATG14 (Park *et al*, 2016; Wold *et al*, 2016), and ATG9 (Papinski *et al*, 2014), and contributes to the initiation of autophagosome formation (Noda & Fujioka, 2015; Lin & Hurley, 2016). On the contrary, ULK1 phosphorylates substrates that are not directly involved in autophagosome formation, such as SEC16A (Joo *et al*, 2016), glycolytic enzymes (Li *et al*, 2016), and STING (Konno *et al*, 2013). p62 is also a member of this category and is closely involved in LLPS, and the p62 body formation (Sanchez-Martin *et al*, 2019). In this study, we showed that ULK1 localized to p62 bodies (Fig 2) and phosphorylated Ser349 of p62 (Fig 1), the latter of which is required for KEAP1 localization and retention to p62 bodies and subsequent NRF2 activation (Figs 3 and 4). Thus, ULK1 modulates the formation and degradation of p62 bodies and also plays a role in the antioxidative-stress response.

When does ULK1 phosphorylate p62? Since ULK1 was localized in p62 bodies both *in vitro* and *in vivo* (Fig 2), it is plausible that ULK1 phosphorylates Ser349 of p62 located in p62 bodies. Indeed, we observed increased S349-phosphorylation in the p62$^{S403E\ S407E}$ mutant, which promotes the LLPS of p62 (Appendix Fig S2). How does ULK1 recognize p62 bodies? Our HS-AFM experiments showed that the p62 homodimer directly bound to ULK1 via dynamic IDR-IDR and IDR-globular domain interactions (Fig 1D). It is known that IDRs specifically interact with multiple target molecules through a binding mode called "coupled folding and binding" (Sugase *et al*, 2007). This binding mode may facilitate conformational changes and phosphorylation of large numbers of p62 molecules in p62 bodies, because substitutions between IDRs that bind to target molecules occur very rapidly (Wright & Dyson, 2015). There is no highly conserved amino acid sequence region among the IDRs of ULK1, ULK2, and Atg1 (data not shown). As shown by HS-AFM analysis (Fig 1D), IDR-mediated interaction between ULK1 and p62 is transient and rather weak. In such cases, it is generally difficult to find conserved binding sequences and motifs due to the extremely low sequence identity. With the phosphomimetic p62 mutant p62^{S349E}, influx of KEAP1 into p62 bodies predominated over efflux (Fig 4E and F). The coexpression of p62^{S349E} and KEAP1 in *p62 KEAP1* double-knockout Huh-1 cells reduced the circularity of p62 bodies compared with the expression of p62^{S349E} alone (Fig 4A and B), and also decreased the fluidity of KEAP1 molecules within p62 bodies (Fig 4G). When the sequestration of KEAP1 within p62 bodies surpasses a certain threshold level, these bodies convert from liquid-like to gel-like droplets. What does this mean? Since autophagy is known to target gel-like rather than liquid-like droplets (Zhang *et al*, 2018; Yamasaki *et al*, 2020; Kageyama *et al*, 2021), it is possible that incorporation of a certain number of KEAP1 molecules into p62 bodies changes them into gel-like aggregates and enhances autophagic degradation. This is consistent with two findings: adding KEAP1 to p62 condensates consisting of p62^{S349E} resulted in amorphous aggregates *in vitro* (Fig 4D), and *p62*$^{S351E/+}$ mice had reduced levels of not only Ser403-phosphorylated p62 representing p62 bodies but also KEAP1 (Fig 5F). Once p62 bodies are degraded by autophagy, the interaction between Ser349-phosphorylated p62 and KEAP1 should be suppressed because Ser349 phosphorylation of p62 occurs mainly in p62 bodies. As a result, KEAP1 remains in the cytoplasm, and NRF2 is degraded. In other words, the retention of KEAP1 in p62 bodies above a threshold level is thought to suppress NRF2 activation in a feedback regulation process.

Nrf2$^{-/-}$ mice grow normally and are fertile (Itoh *et al*, 1997), though they are susceptible to oxidative stress and reactive electrophiles (Yamamoto *et al*, 2018). In addition, they show tooth decolorization due to defective iron transport in the enamel (Yanagawa *et al*, 2004), which makes them easily distinguishable from wild-

© 2023 The Authors

type and heterozygous mice. *p62*$^{S351A/S351A}$, the phosphodefective *p62* knock-in mice in which p62-mediated NRF2 activation should be impaired, were also fertile and did not differ from wild-type mice for 1 year, at least under specific pathogen-free conditions (Fig EV5). However, their incisors were brownish-yellow, in contrast to the grayish white incisors in *Nrf2*-deficient mice (data not shown), indicating that *p62*$^{S351A/S351A}$ mice retain NRF2 activity. p62-mediated NRF2 activation was not required for development or survival, at least under steady-state conditions. The redox-independent antioxidative stress response might have an anti-aging effect since p62 bodies are thought to increase when the activities of both autophagy-lysosomes and the ubiquitin-proteasome system decrease with aging. Further research is needed to determine whether the redox-independent stress response is activated with aging, and if so, which tissues are affected.

In sharp contrast to *p62*$^{S351A/S351A}$ mice, the phosphomimetic *p62* knock-in mice *p62*$^{S351E/+}$, in which p62-mediated NRF2 activation is persistently activated, showed severe phenotypes. The mice had impaired nutritional intake due to hyperkeratosis in the esophagus and forestomach, which led to malnutrition and dehydration (Fig 5G–I). This represented almost a phenocopy of *Keap1*-deficient mice, which exhibit hyperactivation of NRF2 and show hyperkeratosis in the esophagus and forestomach (Wakabayashi *et al*, 2003). One difference is that *p62*$^{S351E/+}$ mice do not develop skin hyperkeratosis, which is observed in *Keap1*-knockout mice (Wakabayashi *et al*, 2003). Why does constant activation of NRF2, which has an inherently cytoprotective role, cause a severe phenotype? The esophagus and stomach are exposed to a variety of toxic foods and drinks. This may cause wounds that require NRF2 for healing, and a redox-independent p62-mediated pathway may be at work. Meanwhile, the healing of skin wounds may be mediated by redox-dependent NRF2 activation (Braun *et al*, 2002). It is plausible that transient activation of NRF2 in response to toxicity, whether redox dependent or independent, is important for biological defense, and that persistent activation leads to inordinate defense responses (e.g., excessive keratinization). In the case of redox-independent stress responses, transient activation of NRF2 is presumably regulated by phosphorylation, dephosphorylation, and autophagic degradation of p62 body.

In conclusion, we showed for first time that the redox-independent NRF2 activation pathway, which is mediated by p62 bodies and their phosphorylation, is physiologically important.

Materials and Methods

Reagents and Tools table

Reagent or resource	Source	Identifier
Antibodies		
Guinea pig polyclonal anti-p62/SQSTM1 (C-terminus)	Progen Biotechnik	Cat#GP62-C; RRID: AB_2687531
Mouse monoclonal anti-p62 Ick ligand	BD Biosciences	Cat#610833; RRID: AB_398152
Rabbit polyclonal anti-p62 (pSer403)	Gene Tex	Cat#GTX128171; RRID: AB_2885723
Rabbit polyclonal anti-p62 (pSer405)	Lim *et al* (2015)	N/A
Rabbit polyclonal anti-p62 (pSer349)	Ichimura *et al* (2013)	N/A
Rabbit polyclonal anti-p62	MBL	Cat#PM045; RRID: AB_1279301
Mouse monoclonal anti-p62	Abnova	Cat#H00008878-M01; RRID: AB_1507408
Rabbit polyclonal anti-KEAP1	Proteintech	Cat#10503-2-AP; RRID: AB_2132625
Rabbit monoclonal anti-ULK1 (D8H5)	Cell Signaling Technology	Cat#8054; RRID: AB_11178668
Rabbit polyclonal anti-ULK2	ABclonal	Cat#NBP-89866; RRID: AB_11009420
Rabbit monoclonal anti-ATG13 (E1Y9V)	Cell Signaling Technology	Cat#13468; RRID: AB_2797419
Rabbit polyclonal anti-ATG13 (pSer318)	Rockland	Cat# 600-401-C49; RRID: AB_11179920
Rabbit polyclonal anti-NRF2 (H-300)	Santa Cruz Biotechnology	Cat#sc-13032; RRID: AB_2263168
Rabbit polyclonal anti-RB1CC1	Proteintech	Cat#17250-1-AP; RRID: AB_10666428
Mouse monoclonal anti-β-actin	Sigma-Aldrich	Cat#A1978; RRID: AB_476692
Mouse monoclonal anti-GAPDH (6C5)	Santa Cruz Biotechnology	Cat#sc-32233; RRID: AB_627679
Mouse monoclonal anti-DDDDK-tag	MBL	Cat#M185-3L; RRID: AB_11123930
Rabbit polyclonal anti-GFP	MBL	Cat#598; RRID: AB_591819
Rabbit polyclonal anti-NQO1	Abcam	Cat#ab9085; RRID: AB_2251526
Rabbit polyclonal anti-UGDH	Abcam	Cat#ab155005
Alexa Fluor Plus 488-conjugated anti-mouse IgG	Thermo Fisher Scientific	Cat#A32766; RRID: AB_2762823
Alexa Fluor 488-conjugated anti-rabbit IgG	Thermo Fisher Scientific	Cat#A11034; RRID: AB_2576217
Alexa Fluor Plus 594-conjugated anti-mouse IgG	Thermo Fisher Scientific	Cat#A32744; RRID: AB_2762826

 © 2023 The Authors

Reagents and Tools table (continued)

Reagent or resource	Source	Identifier
HRP-conjugated goat polyclonal anti-mouse IgG	Jackson ImmunoResearch Laboratories	Cat#115-035-166; RRID: AB_2338511
HRP-conjugated goat polyclonal anti-rabbit IgG	Jackson ImmunoResearch Laboratories	Cat#111-035-144; RRID: AB_2307391
HRP-conjugated goat polyclonal anti-guinea pig IgG	Jackson ImmunoResearch Laboratories	Cat#106-035-003; RRID: AB_2337402
Bacterial and virus strains		
E. coli BL21 (DE3)	Funakoshi	Cat#DS250
E. coli DH5α	Thermo Fisher Scientific	Cat#EC0112
Chemicals		
Lipofectamine 3000 Transfection Reagent	Thermo Fisher Scientific	Cat#L3000015
Lipofectamine RNAiMAX Transfection Reagent	Thermo Fisher Scientific	Cat#13778150
Lipofectamine LTX Reagent with PLUS Reagent	Thermo Fisher Scientific	Cat#15338100
Dnase I	Takara Bio	Cat#2270A
Anti-GFP (Green Fluorescent Protein) mAb-Agarose	MBL	Cat#D153-8
Glutathione Sepharose 4B	GE Healthcare	Cat#17-0756-05
GST-Accept	Nacalai Tesque	Cat#09277-14
PreScission Protease	Cytiva	Cat#27084301
One Step CBB	BIO CRAFT	Cat#CBB-1000
Bafilomycin A_1	KOM	Cat#BVT-0252-M001
Isopropyl β-D-thiogalactopyranoside	Nacalai Tesque	Cat#19742-94
cOmplete EDTA-free (protease inhibitor cocktail)	Roche Applied Science	Cat#05056489001
PhosSTOP (phosphatase inhibitor cocktail)	Roche Applied Science	Cat#4906845001
Polyvinylpyrrolidone	Sigma-Aldrich	Cat#PVP10
Bovine serum albumin	FUJIFILM Wako Pure Chemical Corporation	Cat#016-15091
Protein Kinase A	Sigma-Aldrich	Cat#P5511
Alexa Fluor™ 488 C5 Maleimide	Thermo Fisher Scientific	Cat#A10254
Alexa Fluor™ 647 C2 Maleimide	Thermo Fisher Scientific	Cat#A20347
PD SpinTrap™ G-25	Cytiva	Cat#28918004
Dnase I	Nippon Gene	Cat#314-08071
Ribonuclease	Nippon Gene	Cat#313-01461
Amylose Resin High Flow	New England BioLabs	Cat#E8022
SNAP-Surface Alexa Fluor 488	New England BioLabs	Cat#S9129
SNAP-Surface 649	New England BioLabs	Cat#S9159
Maltose Monohydrate	Nacalai Tesque	Cat#21116-92
Phenylmethylsulfonyl Fluoride	Nacalai Tesque	Cat#27327-52
MRT68921 HCl	Selleck	Cat#S7949
ULK-101	Selleck	Cat#S8793
Dimethyl sulfoxide	Sigma-Aldrich	Cat#D8418
Experimental models: cell lines		
Huh-1	RIKEN	Cat#JCRB0199; RRID: CVCL_2956
Huh-1 *p62* KO	Ichimura *et al* (2013)	N/A
Huh-1 *FIP200* KO	This study	N/A
Huh-1 *p62 KEAP1* DKO	This study	N/A
Huh-1 *ULK1* KO	This study	N/A
HEK293T	ATCC	Cat#CRL-3216
PlatE	Cell BIOLABS	Cat#RV-101
Experimental models: organisms/strains		
Mouse: $p62^{S351A/+}$	This study	N/A

© 2023 The Authors

Reagents and Tools table (continued)

Reagent or resource	Source	Identifier
Mouse: *p62*$^{S351A/S351A}$	This study	N/A
Mouse: *p62*$^{S351E/+}$	This study	N/A
Recombinant DNA		
pGEX6P-1	GE Healthcare	#28954648
pGEX6P-1-8xUb	Genscript	N/A
pGEX6P-KEAP1	This study	N/A
pGEX6P-mCherry-p62	This study	N/A
pGEX6P-mCherry-p62^{S349E}	This study	N/A
pGEX6P-mCherry-p62^{S403E}	This study	N/A
pEGFP-C2	Clontech	Cat#6083-1
pEGFP-C2-p62	This study	N/A
pEGFP-C2-p62^{S349A}	This study	N/A
pEGFP-C2-p62^{S349E}	This study	N/A
pEGFP-C2-p62$^{S403A\ S407A}$	This study	N/A
pEGFP-C2-p62$^{S403E\ S407E}$	This study	N/A
pEGFP-ULK1	This study	N/A
pRetroX-TetOne-Puro-EGFP-p62	This study	N/A
pRetroX-TetOne-Puro-EGFP-p62^{S349E}	This study	N/A
pRetroX-TetOne-Puro-EGFP-p62^{S349A}	This study	N/A
pRetroX-TetOne-Puro-EGFP-p62^{T350A}	This study	N/A
pRetroX-TetOne-Puro-EGFP-LATS1	This study	N/A
pIRES-puro-N3xFLAG	This study	N/A
pIRES-puro-N3xFLAG-ULK1	This study	N/A
pIRES-puro-N3xFLAG-ULK2	This study	N/A
pMAL-c5X	New England BioLabs	Cat#N8108
pMAL-c5X-FIP200 Claw	This study	N/A
pGEX6p-SNAP	This study	N/A
Software and algorithms		
ImageJ	Thermo Fisher Scientific	RRID: SCR_014477
CellPath Finder	Schindelin *et al* (2012)	RRID: SCR_002285
Evolution-Capt Edge	Yokogawa	N/A
FV10-ASW 04.01	Vilber Bio Imaging	N/A
Multi Gauge (version: 3.4)	Fuji Film	N/A
FV31S-SW (version: 2.4.1.198)	Olympus	N/A
Kodec	Olympus	N/A
Biomolecular AFM viewer-2.1	Ngo *et al* (2015)	N/A
GraphPad Prism 9	Amyot and Flechsig (2020)	N/A
Adobe Photoshop CS6	Adobe	N/A

Methods and Protocols

Cell culture

Huh-1 cells (JCRB0199, NIBIOHN) were cultured in Dulbecco's modified Eagle's medium containing 10% fetal bovine serum, 5 U/ml penicillin, and 50 μg/ml streptomycin. For overexpression experiments, Huh-1 cells were transfected using Lipofectamine 3000 (L3000015, Thermo Fisher Scientific, Waltham, MA, USA). Huh-1 cells were authenticated using the STR profile and tested for mycoplasma contamination.

Mice

To generate *p62*^{S351A} knock-in mice, CRISPR RNA (crRNA) was designed to recognize the target site (5′-ACTGGAGTTCACCTG-TAGAT-3′). The synthetic crRNAs (Alt-R CRISPR-Cas9 crRNA), trans-activating CRISPR RNA (tracrRNA) (Alt-R CRISPR-Cas9

 © 2023 The Authors

tracrRNA), and Cas9 protein (Alt-R S.p. Cas9 Nuclease V3) were purchased from Integrated DNA Technologies, Inc. (IDT; Coralville, IA, USA). The 120-mer single-stranded oligodeoxynucleotide (ssODN) carrying the intended base substitutions (TCT to GCC) was synthesized by Eurofins Genomics K.K. (Tokyo, Japan). The CRISPR/Cas9 solution was prepared as previously described (Gurumurthy *et al*, 2019), with minor modifications. Briefly, lyophilized crRNAs and tracrRNA were resuspended in nuclease-free duplex buffer (IDT) to a concentration of 240 μM. Equal volumes of crRNA and tracrRNA were combined, heated at 95°C for 5 min, and then placed in room temperature (RT) for about 10 min to allow formation of crRNA-tracrRNA duplex. Lyophilized ssODN was resuspended in nuclease-free water to a concentration of 4 mg/ml. crRNA-tracrRNA duplex was mixed with Cas9 protein to form a ribonucleoprotein complex, and then mixed with ssODN in Opti-MEM (Thermo Fisher Scientific). The final concentrations of Cas9 protein, crRNA-tracrRNA duplex, and ssODN were 1 μg/ml, 30 μM, and 1 mg/ml, respectively. To induce CRISPR/Cas9-mediated mutation, we applied a method called improved genome editing via oviductal nucleic acid delivery (i-GONAD) (Gurumurthy *et al*, 2019). Approximately 1.5 ml of CRISPR/Cas9 solution was injected into the oviductal lumens of female C57BL/6N mice on day 0.7 of pregnancy. Immediately after the injection, the oviduct regions were grasped with a tweezer-type electrode (catalog no. CUY652-3; Nepa Gene Co., Ltd., Chiba, Japan) and then electroporated using the NEPA21 square-wave pulse generator (Nepa Gene, Chiba, Japan). The electroporation parameters used were previously described (Gurumurthy *et al*, 2019). Pregnant female mice were allowed to deliver their pups. Biopsies of pup tails were performed for genomic DNA isolation, and mutations were validated by sequencing of PCR products amplified from genomic DNAs.

To generate *p62*^{S351E} knock-in mice using mouse embryonic stem (mES) cells, we applied the recently developed prime editing system (Anzalone *et al*, 2019). Details of the methods for establishment of edited mES cells will be published elsewhere. Briefly, we designed prime-editing guide RNA (pegRNA) containing the following sequences: spacer sequence, 5′-GACUGGAGUUCACCUGUAGA-3′; reverse transcription template, 5′-GUGGACCCAGAG-3′; primer-binding site, 5′-ACAGGUGAACUCC-3′. The CAG promoter-driven prime editor 2 (PE2) and the U6 promoter-driven pegRNA expression vectors were originally constructed using pCMV-PE2-P2A-GFP (#132776, Addgene) and the hU6-sgRNA plasmid (Yuza *et al*, 2018). These vectors were co-transfected into RENKA4, a C57BL/6N-derived mES cell line, using Lipofectamine 3000 (Thermo Fisher Scientific). Knock-in mutations in transfected mES clones were validated by sequencing of PCR products amplified from genomic DNAs. Culture of mES cells and generation of chimeric mice were carried out as previously described (Mishina & Sakimura, 2007). Mice were housed in specific pathogen-free facilities, and the Ethics Review Committee for Animal Experimentation of Juntendo University approved the experimental protocol (2022226 and 2022227).

Purification of recombinant protein

mCherry-p62, mCherry-p62 mutants, SNAP-KEAP1, and SNAP-8xUb were prepared as described previously (Kageyama *et al*, 2021). The gene encoding 8xUb was purchased from GenScript, New Jersey, USA. Purified proteins were stored at −80°C until use.

Recombinant SNAP-Atg1 proteins were prepared as described previously (Fujioka *et al*, 2020). To construct the expression plasmid encoding TwinStrep-CS-SNAP-ULK1-His6 (CS; HRV 3C protease recognition site), the genes and pCAG-neo vector (FUJIFILM Wako pure Chemical Corporation, Osaka, Japan) were amplified by PCR. The PCR fragments were assembled using NEBuilder HiFi DNA Assembly Master Mix (New England BioLabs (NEB), Ipswich, MA, USA). The construct was subjected to sequencing analysis to confirm its identity and transfected into Expi293 GnTI cells using Screen *F*ect™ UP-293 (FUJIFILM Wako Pure Chemical Corporation). The cells were collected after 5 days and sonicated in lysis buffer (50 mM Tris–HCl [pH 8.0], 300 mM NaCl, 2 mM $MgCl_2$, 1% Triton X-100, 10% glycerol, 1 mM TCEP, 1× protease inhibitor cocktail (Nacalai Tesque, Kyoto, Japan)) on ice and centrifuged at 16,000 *g* for 40 min at 4°C. The supernatant was purified with a Strep-Tactin-®XT resin column (IBA Lifesciences Göttingen, Germany). The protein was eluted with 20 mM Tris–HCl (pH 8.0), 500 mM NaCl, 50 mM biotin and concentrated using Vivaspin 500 (Cytiva, Marlborough, MA, USA).

Protein Kinase A (PKA) was purchased from Sigma-Aldrich (Darmstadt, Germany). SNAP-tag was expressed in *E. coli* strain BL21 (DE3) using a pGEX6p-SNAP vector and was initially purified using GST-accept resin (Nacalai Tesque). The eluted sample was desalted by Bio-Gel P-6 Desalting Cartridge (BIO-RAD, Hercules, CA, USA) and digested with HRV3C protease at 4°C overnight. After removal of digested GST tag by GST accept resin, the sample was purified by size-exclusion chromatography using Superdex 75 column (GE Healthcare, Chicago, IL, USA) with 20 mM Tris–HCl pH 8.0, 150 mM NaCl. For the expression of MBP-FIP200 Claw, the pMAL-c5X vector (NEB) was selected for production of N-terminal maltose-binding protein (MBP) fusion FIP200 Claw domain (MBP-FIP200 Claw). The sequence encoding DYKDDDDK-tag was inserted in the downstream region of MBP. For construction of the vector (pMAL-c5X-FIP200 Claw), the gene encoding 1490–1594 aa of FIP200 was amplified by PCR and inserted into the downstream region of MBP- DYKDDDDK. Gene insertion was performed by NEBuilder HiFi DNA Assembly (NEB). *E. coli* strain BL21 (DE3) was used for protein expression which was induced by 0.1–0.2 mM IPTG at 18°C for ~20 h. The *E. coli* cells were harvested by centrifugation and lysed by sonication in 500 mM NaCl, 50 mM HEPES-NaOH pH 8.0 supplemented with 1 mM Tris(2-carboxyethyl)phosphine (TCEP), 1 mM phenylmethylsulfonyl fluoride, DNase I (Nippon Gene, Tokyo, Japan), ribonuclease (Nippon Gene) and 1× protease inhibitor cocktail (Nacalai tesque). After removal of insoluble cell debris by centrifugation, the supernatant was applied to amylose resin (NEB). After washing the resin with 500 mM NaCl, 50 mM HEPES-NaOH pH 8.0, MBP-FIP200 Claw was eluted with 10 mM maltose and concentrated to ~400 μM using Amicon Ultra-15 (30,000 NMWL) (Merck Millipore, Burlington, MA, USA). Purified proteins were stored at −80°C until use.

To label PKA and MBP-FIP200 Claw with Alexa Fluor 488 and Alexa Fluor 647, 10 μM PKA and 200 μM MBP-FIP200 Claw in 150 mM NaCl, 20 mM HEPES-NaOH pH 7.0 were reacted with 20 μM Alexa Fluor™ 488 C5 Maleimide and 400 μM Alexa Fluor™ 647 C2 Maleimide (Thermo Fisher Scientific) at 4°C overnight, respectively. After the addition of 100 mM DTT to stop the reaction, fluorescently labeled proteins were separated by PD SpinTrap™ G-25 (Cytiva).

© 2023 The Authors

HS-AFM

The procedure for HS-AFM observation was described previously (Uchihashi *et al*, 2012). HS-AFM images were acquired in tapping mode using a sample-scanning HS-AFM instrument (MS-NEX, Research Institute of Biomolecule Metrology Co., Ltd., Ibaraki, Japan). We used cantilevers measuring ~7 μm long, ~2 μm wide, and ~0.08 μm thick with electron beam-deposited (EBD) tips (tip radius < 10 nm) (USC-F1.2-k0.15, NanoWorld, Neuchâtel, Switzerland). Their resonant frequency and spring constant were 1.2 MHz in air and 0.15 N/m, respectively. Imaging conditions were as follows: scan size, 120 × 120 nm^2 (Figs 1D and EV1A and B) or 150 × 150 nm^2 (Fig EV1C); pixel size, 100 × 100 pixels (Figs 1D and EV1A–C); imaging rate, 8.33 frames/s (Figs 1D and EV1A) or 6.67 frames/s (Fig EV1B and C). Imaging was performed at 23°C. HS-AFM images were viewed and analyzed using the Kodec4.4.7.39 (Ngo *et al*, 2015) and ImageJ software systems.

Sample preparation for HS-AFM imaging

For imaging of SNAP-ULK1 and p62_268–440, SNAP-ULK1 (50 nM) or p62_268–440 (10 nM) was deposited onto freshly cleaved mica glued to the top of a glass stage (diameter, 1.5 mm; height, 2 mm). After incubation for 3–5 min, the mica was rinsed and immersed in the liquid cell containing ~90 μl of imaging buffer A (20 mM NaCl, 20 mM HEPES-NaOH [pH 7.5], 1 mM $MgCl_2$, 0.1 mM ATP) or imaging buffer B (20 mM NaCl, 20 mM HEPES-NaOH [pH 7.5], 1 mM $MgCl_2$), respectively. For imaging of p62_268–440 with SNAP-ULK1 or SNAP-Atg1, 25 nM p62_268–440 and 50 nM SNAP-ULK1 or 10 nM p62_268–440 and 5 nM SNAP-Atg1 in imaging buffer A were mixed in a 0.5-ml tube. The mixed protein solution was deposited onto freshly cleaved mica and incubated for 3–5 min. After rinsing with imaging buffer A, the mica was immersed in ~90 μl of imaging buffer A.

In vitro kinase assay

Purified p62 (268–440 aa), p62 (320–440 aa), or mCherry-p62 was incubated with purified SNAP-Atg1 or SNAP-ULK1 in kinase buffer (20 mM Tris–HCl [pH 7.5], 150 mM NaCl, 0.5 mM $MgCl_2$, 0.1 mM DTT) containing 200 μM of ATP per reaction for 30 min at 37°C. The reaction was terminated by adding LDS sample buffer (NP0007, Thermo Fisher Scientific) and subjected to SDS–PAGE followed by immunoblot analyses with p62 Ser349- (Ichimura *et al*, 2013), Ser403- (GTX128171, GeneTex, Irvine, CA, USA), and Ser407- (Lim *et al*, 2015) specific antibodies.

In vitro LLPS assay

For *in vitro* liquid–liquid phase separation (LLPS) assay, fluorescence observation was performed on glass-bottom dishes (MatTek, El Segundo, CA, USA) coated with 0.3% (w/v) bovine serum albumin using an FV3000RS confocal laser-scanning microscope (Olympus, Tokyo, Japan). 488, 561, and 640-nm lasers were used for excitation of Alexa Fluor 488, mCherry and Alexa Fluor 647/649, respectively. To observe p62-8xUb condensates, mCherry-p62 wild-type or mutants was mixed with SNAP(649)-8xUb (SNAP-8xUb labeled with SNAP-Surface 649). Each final protein concentration was 10 μM. To observe p62-8xUb condensates in the presence of Atg1, ULK1 or negative controls, SNAP(488)-Atg1, SNAP(488)-ULK1 or SNAP(488)-tag (SNAP-Atg1, SNAP-ULK1 or SNAP-tag labeled with SNAP-Surface Alexa Fluor 488) or PKA-Alexa Fluor 488 was premixed with mCherry-p62 wild-type or mutants before mixed with SNAP(649)-8xUb. Final concentration was as follows: SNAP(488)-Atg1/SNAP(488)-ULK1/SNAP(488)-tag/PKA-Alexa Fluor 488, 0.2 μM; SNAP(649)-8xUb, 10 μM; mCherry-p62 wild-type/$p62^{S403E\ S407E}$, 10 μM. To observe p62-8xUb condensates in the presence of KEAP1, SNAP(488)-KEAP1 (SNAP-KEAP1 labeled with SNAP-Surface Alexa Fluor 488) was premixed with mCherry-p62 wild-type or mutants before mixed with SNAP(649)-8xUb. Final concentration was as follows: SNAP(488)-KEAP1, 5 μM; SNAP(649)-8xUb, 10 μM; mCherry-p62 mutants, 10 μM. Buffer solution used for *in vitro* LLPS assay was 200 mM NaCl, 20 mM HEPES-NaOH pH 7.5, 10% glycerol, 1 mM TCEP. Each mixed solution was incubated for 50 min at ~23°C before imaging.

The % area of p62 condensates (the sum of the areas of p62 condensates divided by the total area (106.7 μm × 106.7 μm)) (Fig 2A) was calculated using the "analyze particles" tool of ImageJ software. Statistical analysis was performed by Welch's *t*-test.

Fluorescence microscopy-based competitive binding assay

GST-accept beads (particle size 50–150 μm) was selected as the beads to be coated by GST-tagged mCherry-p62. 2 μl of 50% suspension of GST-accept beads in a PCR tube was washed with 20 μl of Buffer F (150 mM NaCl, 20 mM HEPES-NaOH pH 7.4) three times. Then, 5 μM GST-mCherry-p62 was incubated with the beads in 5 μl of Buffer F for 30 min. After five times washing with 20 μl of Buffer F, 0.4 μM SNAP-ULK1 labeled with Alexa Fluor 488 and 0–40 μM MBP-FIP200 Claw labeled with Alexa Fluor 647 C2 maleimide were incubated with the beads in 5 μl of Buffer F containing 1 mM DTT for 1 h. After five times washing with 20 μl of Buffer F containing 1 mM DTT, the beads were resuspended with 20 μl of Buffer F containing 1 mM DTT. 6 μl of the beads suspension on glass-bottom dish (MatTek) was then imaged using an FV3000RS confocal laser-scanning microscope (Olympus) at ~23°C. Fluorescence intensities of ULK1 and p62 on the beads were measured and analyzed by Fiji (ImageJ).

Immunoblot analysis

Cells were lysed in ice-cold TNE buffer (50 mM Tris–HCl [pH 7.5], 150 mM NaCl, 1 mM EDTA) containing 1% Triton X-100 and cOmplete EDTA-free protease inhibitor cocktail (5056489001, Roche). After centrifugation twice at 15,000 *g* for 10 min, the supernatant was collected as the cell lysates. Protein concentrations were determined by bicinchoninic acid (BCA) protein assay (23225, Thermo Fisher Scientific). The lysate was boiled in LDS sample buffer, and the samples were separated by SDS–PAGE and then transferred to polyvinylidene difluoride membranes. For gene knockdown, cells were transfected with siGENOME siRNA targeting *ULK1* (D-005049-01-0005; 5′-CCUAAAACGUGUCUUAUUU-3′, D-005049-02-0005; 5′-ACUUGUAGGUGUUUAAGAA-3′, D-005049-03-0005; 5′-GGUUAGCCCUGCCUGAAUC-3′, Horizon Discovery, Cambridge, United Kingdom) and *ULK2* (MQ-005396-01-0002; mixtures of sequences 5′-UAAAGGAACUUCAGCAUGA-3′, 5′-GUGGAGACCUCGCAGAUUA-3′, 5′-GAAGAACAGUCGAAAGAUUA-3′, 5′-GCAGACGUGCUUCAAAUGA-3′, Horizon Discovery) or a non-targeting control siRNA (siGENOME Non-Targeting siRNA; mixtures of sequences 5′-UAGCGACUAAACACAUCAA-3′, 5′-UAAGGCUAUGAAGAGAUAC-3′, 5′-AUGUAUUGGCCUGUAUUAG-3′, and 5′-AUGAACGUGAAUUGCUCAA-3′, Horizon Discovery) using DharmaFECT1 (T-2002, Horizon

 © 2023 The Authors

Discovery) and lysed 96 h after transfection in TNE buffer containing 1% SDS. Antibodies against p62 (610832, BD Biosciences, Franklin Lakes, NJ, USA), Ser403-phosphorylated p62 (GTX128171, GeneTex), Ser349-phosphorylated p62 (Ichimura *et al*, 2013), Ser405-phosphorylated p62 (Lim *et al*, 2015), ULK1 (8054, Cell Signaling Technology, Danvers, MA, USA), ULK2 (A15244, ABclonal, Huissen, Netherlands), FIP200 (17250-1-AP, Proteintech Group, Rosemont, IL, USA), and NRF2 (H-300; Santa Cruz Biotechnology, Dallas, TX, USA) were used as primary antibodies. Blots were then incubated with horseradish peroxidase-conjugated secondary antibody (Goat Anti-Mouse IgG (H + L), 115–035-166, Goat Anti-Rabbit IgG (H + L) 111–035-144, and Goat Anti-Guinea Pig IgG (H + L), all from Jackson ImmunoResearch, West Grove, PA, USA) and visualized by chemiluminescence.

Immunofluorescence analysis

Huh-1 cells on coverslips were washed with PBS and fixed with 4% paraformaldehyde (PFA) for 15 min at RT, permeabilized with 0.1% Triton X-100 in PBS for 5 min, and blocked with 0.1% (w/v) gelatin (G9391, Sigma-Aldrich) in PBS for 20 min. Then, cells were incubated with primary antibodies in the blocking buffer for 1 h, washed with PBS, and incubated with secondary antibodies for 1 h. Antibodies against p62 (610832, BD Biosciences), S403-phosphorylated p62 (GTX128171, GeneTex), S349-phosphorylated p62 (Ichimura *et al*, 2013), KEAP1 (10503-2-AP, Proteintech), and ULK1 (8054, Cell Signaling Technology) were used as primary antibodies. Goat anti-Mouse IgG (H + L) Highly Cross-Adsorbed Secondary Antibody, Alexa Fluor 647 (A21236, Thermo Fisher Scientific) and Goat anti-Rabbit IgG (H + L) Cross-Adsorbed Secondary Antibody, Alexa Fluor 488 (A11008, Thermo Fisher Scientific) were used as secondary antibodies. Nuclei were stained with Hoechst 33342 (62249, Thermo Fisher Scientific). Cells were imaged using the FV1000 confocal laser-scanning microscope with FV10-ASW 04.01 (Olympus) and a UPlanSApo ×60 NA 1.40 oil objective lens. Contrast and brightness of images were adjusted using Photoshop 2021v25.0 (Adobe, San Jose, CA, USA). The number, size, and circularity of p62-positive punctae in each cell and the mean fluorescence intensity of each signal on p62-positive punctae were quantified using a Benchtop High-Content Analysis System (CQ1, Yokogawa Electric Corp., Tokyo, Japan) and CellPathfinder software (Yokogawa Electric Corp.).

Correlative light and electron microscopic analysis

Huh-1 cells on coverslips etched with 150-μm grids (CS01885, Matsunami Glass Ind. Osaka, Japan) were transfected with pMRX-IP-GFP-ULK1 or pMRX-IP-GFP-ULK2. After 24 h, cells were fixed with 2% PFA–0.1% glutaraldehyde (GA) in 0.1 M PB (pH 7.4). Then, phase-contrast and fluorescence images were obtained using a confocal microscope (FV1000). After image acquisition, the cells were fixed again with 2% PFA and 2% GA in 0.1 M PB (pH 7.4), processed according to the reduced-osmium method (Arai & Waguri, 2019), and embedded in Epon812. Areas containing cells of interest were trimmed, cut as serial 80-nm sections, and observed using an electron microscope (EM; JEM1400; JEOL, Tokyo, Japan). Light microscopy and EM images were aligned according to three p62 bodies using Photoshop CS6 (Adobe).

Histological analyses

Mouse livers were excised, cut into small pieces, and fixed by immersion in 4% PFA–4% sucrose in 0.1 M PB, pH 7.4. After rinsing, they were embedded in paraffin for immunostaining. Paraffin sections of 3-μm thickness were prepared and processed for HE staining or IHC. For IHC, antigen retrieval was performed for 20 min at 98°C using a microwave processor (MI-77, AZUMAYA, Tokyo, Japan) in 1% immunosaver (Nissin EM, Tokyo, Japan). Sections were blocked and incubated for 2 days at 4°C with the following primary antibodies: rabbit polyclonal antibody against NQO1 (Abcam), followed by N-Histofine simple stain mouse MAX PO kit (NICHIREI BIOSCIENCES, Tokyo, Japan) using 3,39-diaminobenzidine. Images of the stained specimens were acquired with a microscope (BX51, Olympus) equipped with a cooled CCD camera system (DP-71, Olympus).

FLAP and FLIP assays

p62/KEAP1 double-knockout Huh-1 cells expressing GFP-p62^{S349E} or GFP-p62^{S349A} in a doxycycline treatment-dependent manner were generated using a reverse tet-regulated retroviral vector, as previously reported. To induce the expression of GFP-p62^{S349E} or GFP-p62^{S349A}, the cells were treated with 50 ng/ml of doxycycline (Dox, Sigma-Aldrich) for 24 h. Thereafter, m Cherry-KEAP1 was transfected with Lipofectamine 3000 (Thermo Fisher Scientific) and cultured for 24 h. In FRAP assays, GFP-p62 bodies that were positive for mCherry-KEAP1 were bleached using a laser intensity of 10% at 488 nm, and then the fluorescence recovery of mCherry was recorded. In FLIP assays, around 80% of the total cell area was set as the region of interest for photobleaching (excitation output level: 10% at 561 nm; iterations: 3–5) using FV31S-SW software (Olympus), and then the fluorescence loss of mCherry-KEAP1 in GFP-p62^{S349E} or GFP-p62^{S349A} bodies was recorded. The fluorescence intensity of mCherry-KEAP1 within the p62 bodies in the photobleaching area recovered to 32% at 15 min after photobleaching and reached equilibrium. Therefore, the fluorescence intensity of mCherry-KEAP1 within the p62 bodies in the nonphotobleaching area was measured at 30 min after fluorescence loss. Olympus FV31S-SW software (version: 2.4.1.198) and cellSens Dimension Desktop 3.2 (Build 23706) was used for image collection and analysis. The mobile fraction was calculated from 10 measurements by the following equation: $Mf = (F\infty - F0)/(Fi - F0)$, where Mf is the mobile fraction, $F\infty$ is the fluorescence intensity after full recovery (plateau), Fi is the initial fluorescence intensity prior to bleaching, and F0 is the fluorescence intensity immediately after bleaching. The half-time (*t50*) of fluorescence recovery was calculated from 10 measurements by curve fitting using the one-phase decay model of GraphPad PRISM 9 (GraphPad Software, San Diego, CA, USA).

RNA sequencing (RNA-seq)

Total RNA from livers of *p62*$^{+/+}$ and *p62*$^{S351E/+}$ mice at P19 was extracted using the RNeasy Mini Kit (Qiagen, Hulsterweg, Netherlands). Ribosomal RNA was depleted using a NEBNext rRNA Depletion Kit (NEB). For sequencing, a cDNA library was synthesized using the NEBNext Ultra II RNA Library Prep Kit for Illumina (NEB). Sequencing was performed on a NextSeq 500 sequencer (Illumina, San Diego, CA, USA) with 75-bp single-end reads. Resulting reads were mapped to the UCSC (University of California, Santa Cruz, CA, USA) mm10 reference genome using the Spliced Transcripts

© 2023 The Authors

Alignment to a Reference (STAR) Aligner. The number of reads was calculated using RNA-Seq by Expectation Maximization (RSEM), and differentially expressed genes (DEGs) between $p62^{+/+}$ and $p62^{S351E/+}$ mice were analyzed by DESeq2. DEGs were visualized by volcano plots.

Quantitative real-time PCR (qRT-PCR)

cDNAs were synthesized with 1 μg of total RNA using FastGene Scriptase Basic cDNA Synthesis (NE-LS62, NIPPON Genetics, Tokyo, Japan). qRT-PCR was performed with TaqMan® Fast Advanced Master Mix (444556, Thermo Fisher Scientific) on a QuantStudio™ 6 Pro (A43180, Thermo Fisher Scientific). Signals were normalized against *Gusb* (β-glucuronidase). Predesigned TaqMan Gene Expression Assays, including primer sets and TaqMan probes (Gusb; Mm01197698_m1, Nqo1; Mm01253561_m1, Ugdh; Mm00447643_m1 and Gstm1; Mm00833915_g1, GAPDH; Hs02786624_g1, NQO1; Hs00168547_m1, UGDH; Hs01097550_m1, GCLC; Hs00155249_m1, SOD1; Hs00533490_m1, SQSTM1; Hs00177654_m1) were purchased from Thermo Fisher Scientific.

Statistical analysis

Statistical analyses were performed using the unpaired *t*-test (Welch *t*-test), Tukey's test, or Šidák's multiple comparison test after one-way ANOVA. GraphPad PRISM 9 (GraphPad Software) was used for the statistical analyses. All tests were two-sided, and *P*-values of < 0.05 were considered statistically significant.

Data availability

The RNA-seq data (GSE229713) is currently open in Gene Expression Omnibus (https://www.ncbi.nlm.nih.gov/geo/).

Expanded View for this article is available online.

Acknowledgements

We thank Dr. Mikako Shirouzu for providing purified p62 (268-440aa) and p62 (320-440aa) proteins and Ms. Miyako Yoshimura for technical assistance. We also thank Mr. Katsuyuki Kanno, and Mr. Takayuki Yabe for their help with CLEM and histological analyses. This work was supported by JSPS KAKENHI Grant Number JP19H05706, JP21H004771 (to M.K.); JP19H05707 (to N.N.N.); JP20K06644 (to Y.I.); JP20H03415 (to S.W.); JP19K16344 (to D.N.); JP21H05731 (to Y.F.); JP20H03213 (to H.M.); JP20K06549 (to S.K.); JP21K06178 (to T.F.); JP21H04163 (to S.K-H.); JP22K06300 (to R.A.); Advanced Research and Development Programs for Medical Innovation (AMED-CREST, PRIME) Grant Number JP22gm1410004h0003 (to M.K.); JP20gm6410009 (to Y.F.); JP21gm6410019h0001 (to H.M.); JST CREST Grant Number JPMJCR20E3 (to N.N.N.); the Japan Society for the Promotion of Science (an A3 foresight program) (to M.K.). This work was also supported by the Takeda Science Foundation (to D.N., N.N.N., and M.K.); Inamori foundation (to H.M.).

Author contributions

Masaaki Komatsu: Conceptualization; data curation; supervision; funding acquisition; writing – original draft; writing – review and editing. **Ryo Ikeda:** Data curation; formal analysis; investigation; writing – review and editing. **Daisuke Noshiro:** Formal analysis; funding acquisition; investigation; writing – review and editing. **Hideaki Morishita:** Data curation; formal analysis; funding acquisition; investigation; writing – review and editing. **Shuhei Takada:** Formal analysis; investigation. **Shun Kageyama:** Formal analysis; funding acquisition; investigation. **Yuko Fujioka:** Formal analysis; investigation. **Tomoko Funakoshi:** Formal analysis; funding acquisition; investigation; writing – review and editing. **Satoko Komatsu-Hirota:** Formal analysis; funding acquisition; investigation. **Ritsuko Arai:** Formal analysis. **Elena Ryzhii:** Formal analysis. **Manabu Abe:** Resources; writing – review and editing. **Hozumi Motohashi:** Data curation; formal analysis; supervision. **Tomoaki Koga:** Data curation; formal analysis; writing – review and editing. **Mitsuyoshi Nakao:** Supervision. **Kenji Sakimura:** Supervision. **Arata Horii:** Supervision. **Satoshi Waguri:** Data curation; formal analysis; supervision; investigation; writing – review and editing. **Yoshinobu Ichimura:** Data curation; formal analysis; investigation; writing – review and editing. **Nobuo N Noda:** Conceptualization; data curation; formal analysis; supervision; funding acquisition; investigation; writing – review and editing.

Disclosure and competing interests statement

The authors declare that they have no conflict of interest.

References

Agudo-Canalejo J, Schultz SW, Chino H, Migliano SM, Saito C, Koyama-Honda I, Stenmark H, Brech A, May AI, Mizushima N *et al* (2021) Wetting regulates autophagy of phase-separated compartments and the cytosol. *Nature* 591: 142 – 146

Alberti S, Hyman AA (2021) Biomolecular condensates at the nexus of cellular stress, protein aggregation disease and ageing. *Nat Rev Mol Cell Biol* 22: 196 – 213

Amyot R, Flechsig H (2020) BioAFMviewer: an interactive interface for simulated AFM scanning of biomolecular structures and dynamics. *PLoS Comput Biol* 16: e1008444

Anzalone AV, Randolph PB, Davis JR, Sousa AA, Koblan LW, Levy JM, Chen PJ, Wilson C, Newby GA, Raguram A *et al* (2019) Search-and-replace genome editing without double-strand breaks or donor DNA. *Nature* 576: 149 – 157

Arai R, Waguri S (2019) Improved electron microscopy fixation methods for tracking autophagy-associated membranes in cultured mammalian cells. *Methods Mol Biol* 1880: 211 – 221

Braun S, Hanselmann C, Gassmann MG, auf dem Keller U, Born-Berclaz C, Chan K, Kan YW, Werner S (2002) Nrf2 transcription factor, a novel target of keratinocyte growth factor action which regulates gene expression and inflammation in the healing skin wound. *Mol Cell Biol* 22: 5492 – 5505

Cuadrado A, Rojo AI, Wells G, Hayes JD, Cousin SP, Rumsey WL, Attucks OC, Franklin S, Levonen AL, Kensler TW *et al* (2019) Therapeutic targeting of the NRF2 and KEAP1 partnership in chronic diseases. *Nat Rev Drug Discov* 18: 295 – 317

Faruk MO, Ichimura Y, Kageyama S, Komatsu-Hirota S, El-Gowily AH, Sou YS, Koike M, Noda NN, Komatsu M (2021a) Phase-separated protein droplets of amyotrophic lateral sclerosis-associated p62/SQSTM1 mutants show reduced inner fluidity. *J Biol Chem* 297: 101405

Faruk MO, Ichimura Y, Komatsu M (2021b) Selective autophagy. *Cancer Sci* 112: 3972 – 3978

Fujioka Y, Alam JM, Noshiro D, Mouri K, Ando T, Okada Y, May AI, Knorr RL, Suzuki K, Ohsumi Y *et al* (2020) Phase separation organizes the site of autophagosome formation. *Nature* 578: 301 – 305

Gurumurthy CB, Sato M, Nakamura A, Inui M, Kawano N, Islam MA, Ogiwara S, Takabayashi S, Matsuyama M, Nakagawa S *et al* (2019) Creation of CRISPR-based germline-genome-engineered mice without *ex vivo* handling of zygotes by i-GONAD. *Nat Protoc* 14: 2452 – 2482

 © 2023 The Authors

Ichimura Y, Waguri S, Sou YS, Kageyama S, Hasegawa J, Ishimura R, Saito T, Yang Y, Kouno T, Fukutomi T *et al* (2013) Phosphorylation of p62 activates the Keap1-Nrf2 pathway during selective autophagy. *Mol Cell* 51: 618 – 631

Ishikawa-Ankerhold HC, Ankerhold R, Drummen GP (2012) Advanced fluorescence microscopy techniques–FRAP, FLIP, FLAP, FRET and FLIM. *Molecules* 17: 4047 – 4132

Isogai S, Morimoto D, Arita K, Unzai S, Tenno T, Hasegawa J, Sou YS, Komatsu M, Tanaka K, Shirakawa M *et al* (2011) Crystal structure of the ubiquitin-associated (UBA) domain of p62 and its interaction with ubiquitin. *J Biol Chem* 286: 31864 – 31874

Itoh K, Chiba T, Takahashi S, Ishii T, Igarashi K, Katoh Y, Oyake T, Hayashi N, Satoh K, Hatayama I *et al* (1997) An Nrf2/small Maf heterodimer mediates the induction of phase II detoxifying enzyme genes through antioxidant response elements. *Biochem Biophys Res Commun* 236: 313 – 322

Jakobi AJ, Huber ST, Mortensen SA, Schultz SW, Palara A, Kuhm T, Shrestha BK, Lamark T, Hagen WJH, Wilmanns M *et al* (2020) Structural basis of p62/SQSTM1 helical filaments and their role in cellular cargo uptake. *Nat Commun* 11: 440

Joo JH, Wang B, Frankel E, Ge L, Xu L, Iyengar R, Li-Harms X, Wright C, Shaw TI, Lindsten T *et al* (2016) The noncanonical role of ULK/ATG1 in ER-to-Golgi trafficking is essential for cellular homeostasis. *Mol Cell* 62: 491 – 506

Kageyama S, Gudmundsson SR, Sou YS, Ichimura Y, Tamura N, Kazuno S, Ueno T, Miura Y, Noshiro D, Abe M *et al* (2021) p62/SQSTM1-droplet serves as a platform for autophagosome formation and anti-oxidative stress response. *Nat Commun* 12: 16

Kehl SR, Soos BA, Saha B, Choi SW, Herren AW, Johansen T, Mandell MA (2019) TAK1 converts Sequestosome 1/p62 from an autophagy receptor to a signaling platform. *EMBO Rep* 20: e46238

Kirkin V, Rogov VV (2019) A diversity of selective autophagy receptors determines the specificity of the autophagy pathway. *Mol Cell* 76: 268 – 285

Kodera N, Noshiro D, Dora SK, Mori T, Habchi J, Blocquel D, Gruet A, Dosnon M, Salladini E, Bignon C *et al* (2021) Structural and dynamics analysis of intrinsically disordered proteins by high-speed atomic force microscopy. *Nat Nanotechnol* 16: 181 – 189

Komatsu M, Kurokawa H, Waguri S, Taguchi K, Kobayashi A, Ichimura Y, Sou YS, Ueno I, Sakamoto A, Tong KI *et al* (2010) The selective autophagy substrate p62 activates the stress responsive transcription factor Nrf2 through inactivation of Keap1. *Nat Cell Biol* 12: 213 – 223

Konno H, Konno K, Barber GN (2013) Cyclic dinucleotides trigger ULK1 (ATG1) phosphorylation of STING to prevent sustained innate immune signaling. *Cell* 155: 688 – 698

Li TY, Sun Y, Liang Y, Liu Q, Shi Y, Zhang CS, Zhang C, Song L, Zhang P, Zhang X *et al* (2016) ULK1/2 constitute a bifurcate node controlling glucose metabolic fluxes in addition to autophagy. *Mol Cell* 62: 359 – 370

Lim J, Lachenmayer ML, Wu S, Liu W, Kundu M, Wang R, Komatsu M, Oh YJ, Zhao Y, Yue Z (2015) Proteotoxic stress induces phosphorylation of p62/SQSTM1 by ULK1 to regulate selective autophagic clearance of protein aggregates. *PLoS Genet* 11: e1004987

Lin MG, Hurley JH (2016) Structure and function of the ULK1 complex in autophagy. *Curr Opin Cell Biol* 39: 61 – 68

Martin KR, Celano SL, Solitro AR, Gunaydin H, Scott M, O'Hagan RC, Shumway SD, Fuller P, MacKeigan JP (2018) A potent and selective ULK1 inhibitor suppresses autophagy and sensitizes cancer cells to nutrient stress. *iScience* 8: 74 – 84

Matsumoto G, Wada K, Okuno M, Kurosawa M, Nukina N (2011) Serine 403 phosphorylation of p62/SQSTM1 regulates selective autophagic clearance of ubiquitinated proteins. *Mol Cell* 44: 279 – 289

Mishina M, Sakimura K (2007) Conditional gene targeting on the pure C57BL/6 genetic background. *Neurosci Res* 58: 105 – 112

Ngo KX, Kodera N, Katayama E, Ando T, Uyeda TQ (2015) Cofilin-induced unidirectional cooperative conformational changes in actin filaments revealed by high-speed atomic force microscopy. *Elife* 4: e04806

Noda NN, Fujioka Y (2015) Atg1 family kinases in autophagy initiation. *Cell Mol Life Sci* 72: 3083 – 3096

Noda NN, Wang Z, Zhang H (2020) Liquid-liquid phase separation in autophagy. *J Cell Biol* 219: e202004062

Papinski D, Schuschnig M, Reiter W, Wilhelm L, Barnes CA, Maiolica A, Hansmann I, Pfaffenwimmer T, Kijanska M, Stoffel I *et al* (2014) Early steps in autophagy depend on direct phosphorylation of Atg9 by the Atg1 kinase. *Mol Cell* 53: 471 – 483

Park JM, Jung CH, Seo M, Otto NM, Grunwald D, Kim KH, Moriarity B, Kim YM, Starker C, Nho RS *et al* (2016) The ULK1 complex mediates MTORC1 signaling to the autophagy initiation machinery via binding and phosphorylating ATG14. *Autophagy* 12: 547 – 564

Petherick KJ, Conway OJ, Mpamhanga C, Osborne SA, Kamal A, Saxty B, Ganley IG (2015) Pharmacological inhibition of ULK1 kinase blocks mammalian target of rapamycin (mTOR)-dependent autophagy. *J Biol Chem* 290: 11376 – 11383

Pilli M, Arko-Mensah J, Ponpuak M, Roberts E, Master S, Mandell MA, Dupont N, Ornatowski W, Jiang S, Bradfute SB *et al* (2012) TBK-1 promotes autophagy-mediated antimicrobial defense by controlling autophagosome maturation. *Immunity* 37: 223 – 234

Reits EA, Neefjes JJ (2001) From fixed to FRAP: measuring protein mobility and activity in living cells. *Nat Cell Biol* 3: E145 – E147

Ro SH, Semple IA, Park H, Park H, Park HW, Kim M, Kim JS, Lee JH (2014) Sestrin2 promotes Unc-51-like kinase 1 mediated phosphorylation of p62/sequestosome-1. *FEBS J* 281: 3816 – 3827

Russell RC, Tian Y, Yuan H, Park HW, Chang YY, Kim J, Kim H, Neufeld TP, Dillin A, Guan KL (2013) ULK1 induces autophagy by phosphorylating Beclin-1 and activating VPS34 lipid kinase. *Nat Cell Biol* 15: 741 – 750

Sanchez-Martin P, Saito T, Komatsu M (2019) p62/SQSTM1: 'Jack of all trades' in health and cancer. *FEBS J* 286: 8 – 23

Schindelin J, Arganda-Carreras I, Frise E, Kaynig V, Longair M, Pietzsch T, Preibisch S, Rueden C, Saalfeld S, Schmid B *et al* (2012) Fiji: an open-source platform for biological-image analysis. *Nat Methods* 9: 676 – 682

Strom AR, Emelyanov AV, Mir M, Fyodorov DV, Darzacq X, Karpen GH (2017) Phase separation drives heterochromatin domain formation. *Nature* 547: 241 – 245

Sugase K, Dyson HJ, Wright PE (2007) Mechanism of coupled folding and binding of an intrinsically disordered protein. *Nature* 447: 1021 – 1025

Sun D, Wu R, Zheng J, Li P, Yu L (2018) Polyubiquitin chain-induced p62 phase separation drives autophagic cargo segregation. *Cell Res* 28: 405 – 415

Taguchi K, Fujikawa N, Komatsu M, Ishii T, Unno M, Akaike T, Motohashi H, Yamamoto M (2012) Keap1 degradation by autophagy for the maintenance of redox homeostasis. *Proc Natl Acad Sci USA* 109: 13561 – 13566

Turco E, Witt M, Abert C, Bock-Bierbaum T, Su MY, Trapannone R, Sztacho M, Danieli A, Shi X, Zaffagnini G *et al* (2019) FIP200 claw domain binding to p62 promotes autophagosome formation at ubiquitin condensates. *Mol Cell* 74: 330 – 346

Turco E, Savova A, Gere F, Ferrari L, Romanov J, Schuschnig M, Martens S (2021) Reconstitution defines the roles of p62, NBR1 and TAX1BP1 in

© 2023 The Authors

ubiquitin condensate formation and autophagy initiation. *Nat Commun* 12: 5212

Uchihashi T, Kodera N, Ando T (2012) Guide to video recording of structure dynamics and dynamic processes of proteins by high-speed atomic force microscopy. *Nat Protoc* 7: 1193 – 1206

Wakabayashi N, Itoh K, Wakabayashi J, Motohashi H, Noda S, Takahashi S, Imakado S, Kotsuji T, Otsuka F, Roop DR *et al* (2003) Keap1-null mutation leads to postnatal lethality due to constitutive Nrf2 activation. *Nat Genet* 35: 238 – 245

Wold MS, Lim J, Lachance V, Deng Z, Yue Z (2016) ULK1-mediated phosphorylation of ATG14 promotes autophagy and is impaired in Huntington's disease models. *Mol Neurodegener* 11: 76

Woodruff JB, Hyman AA, Boke E (2018) Organization and function of non-dynamic biomolecular condensates. *Trends Biochem Sci* 43: 81 – 94

Wright PE, Dyson HJ (2015) Intrinsically disordered proteins in cellular signalling and regulation. *Nat Rev Mol Cell Biol* 16: 18 – 29

Yamamoto H, Fujioka Y, Suzuki SW, Noshiro D, Suzuki H, Kondo-Kakuta C, Kimura Y, Hirano H, Ando T, Noda NN *et al* (2016) The intrinsically disordered protein Atg13 mediates supramolecular assembly of autophagy initiation complexes. *Dev Cell* 38: 86 – 99

Yamamoto M, Kensler TW, Motohashi H (2018) The KEAP1-NRF2 system: a thiol-based sensor-effector apparatus for maintaining redox homeostasis. *Physiol Rev* 98: 1169 – 1203

Yamasaki A, Alam JM, Noshiro D, Hirata E, Fujioka Y, Suzuki K, Ohsumi Y, Noda NN (2020) Liquidity is a critical determinant for selective autophagy of protein condensates. *Mol Cell 77*: 1163 – 1175

Yanagawa T, Itoh K, Uwayama J, Shibata Y, Yamaguchi A, Sano T, Ishii T, Yoshida H, Yamamoto M (2004) Nrf2 deficiency causes tooth decolourization due to iron transport disorder in enamel organ. *Genes Cells* 9: 641 – 651

Yuza K, Nakajima M, Nagahashi M, Tsuchida J, Hirose Y, Miura K, Tajima Y, Abe M, Sakimura K, Takabe K *et al* (2018) Different roles of sphingosine kinase 1 and 2 in pancreatic cancer progression. *J Surg Res* 232: 186 – 194

Zaffagnini G, Savova A, Danieli A, Romanov J, Tremel S, Ebner M, Peterbauer T, Sztacho M, Trapannone R, Tarafder AK *et al* (2018) p62 filaments capture and present ubiquitinated cargos for autophagy. *EMBO J* 37: e98308

Zhang G, Wang Z, Du Z, Zhang H (2018) mTOR regulates phase separation of PGL granules to modulate their autophagic degradation. *Cell* 174: 1492 – 1506

License: This is an open access article under the terms of the Creative Commons Attribution License, which permits use, distribution and reproduction in any medium, provided the original work is properly cited.

 © 2023 The Authors